

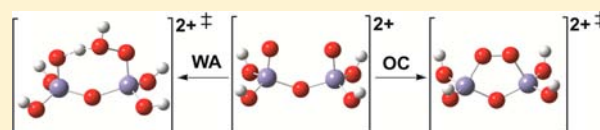
Studies of the Di-iron(VI) Intermediate in Ferrate-Dependent Oxygen Evolution from Water

Rupam Sarma, Alfredo M. Angeles-Boza, David W. Brinkley, and Justine P. Roth*

Department of Chemistry, Johns Hopkins University, 3400 North Charles Street, Baltimore, Maryland 21218, United States

S Supporting Information

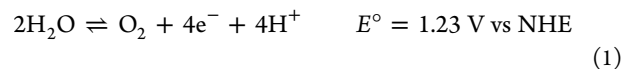
ABSTRACT: Molecular oxygen is produced from water via the following reaction of potassium ferrate (K_2FeO_4) in acidic solution: $4[\text{H}_3\text{Fe}^{\text{VI}}\text{O}_4]^+ + 8\text{H}_3\text{O}^+ \rightarrow 4\text{Fe}^{3+} + 3\text{O}_2 + 18\text{H}_2\text{O}$. This study focuses upon the mechanism by which the O–O bond is formed. Stopped-flow kinetics at variable acidities in H_2O and D_2O are used to complement the analysis of competitive oxygen-18 kinetic



isotope effects (^{18}O KIEs) upon consumption of *natural abundance* water. The derived ^{18}O KIEs provide insights concerning the identity of the transition state. Water attack (WA) and oxo-coupling (OC) transition states were evaluated for various reactions of monomeric and dimeric ferrates using a calibrated density functional theory protocol. Vibrational frequencies from optimized isotopic structures are used here to predict ^{18}O KIEs for comparison to experimental values determined using an established competitive isotope-fractionation method. The high level of agreement between experimental and theoretic isotope effects points to an intramolecular OC mechanism within a di-iron(VI) intermediate, consistent with the analysis of the reaction kinetics. Alternative mechanisms are excluded based on insurmountably high free energy barriers and disagreement with calculated ^{18}O KIEs.

INTRODUCTION

The “splitting” of water into oxygen and hydrogen equivalents by eq 1 is central to life on earth where oxygenic photosynthesis provides the reducing equivalents required for the fixation of CO_2 .¹ The promise of “solar hydrogen” as a clean-burning fuel has made “artificial photosynthesis” a major research objective.² There is a consensus that such approaches are needed to fend off a looming energy crisis,³ the effects of global warming,⁴ and the devastation of natural environments caused by mining fossil fuels.⁵ Alternative technologies are being designed to use photon-absorbing materials that can effect light to energy transduction, as in photosynthetic organisms that subsist in aerobic environments.^{2,6} Presently, there is a need to illuminate the chemical mechanisms of water oxidation with respect to the O–O bond forming step so that more efficient catalysts can be designed to produce hydrogen gas as an economically viable alternative to fossil fuels. The present study focuses upon a testable experimental and theoretical model reaction.



Research over the past decade has led to the discovery of homogeneous water oxidation catalysts⁷ that mediate eq 1, albeit at high overpotentials. To improve catalyst design, it is imperative to understand the origins of the large kinetic barriers, which require large driving forces for H_2O oxidation to occur at appreciable rates. Some lines of evidence suggest that such barriers, in homogeneous systems, reflect rate-limiting O–O bond formation, while others propose kinetic control by steps upstream or downstream, prior to release of O_2 .^{7,8k}

Computational investigations of synthetic systems have suggested that coupling of two oxygen nuclei can occur through ligands bound to transition metal centers with open-shell/radical character or water attack reactions, which involve high-energy electrophilic intermediates.^{8,9}

In this study, we outline the use of oxygen-18 kinetic isotope effects (^{18}O KIEs) as a probe of O–O bond-forming mechanisms, which is useful in relating theory to experiment, thus, providing calibration of modeling efforts. Isotope labeling experiments have historically provided fundamental insights in this area;¹⁰ however, when water exchange rates are rapid, the discrimination between intramolecular and intermolecular pathways becomes exceedingly difficult.

Recently, we outlined an approach wherein competitive oxygen-18 isotope fractionation¹¹ of *natural abundance* water was applied to investigate water oxidation catalysis.¹² Here we present combined experimental and computational studies of a unique stoichiometric reaction wherein potassium ferrate ($\text{K}_2\text{Fe}^{\text{VI}}\text{O}_4$) mediates an O–O bond-forming reaction that can be examined in isolation; this is rarely the case for catalytic reactions because multiple redox steps precede and can obscure this critical step. As a complement to the interrogation of ^{18}O KIEs experimentally and computationally, at the density functional level of theory (DFT), stopped-flow kinetics and spectroscopic measurements are also presented. The objective of this work is to test whether heavy atom isotope effects can be predicted based on the changes of isotopic vibrational frequencies that characterize specific transition states consistent

Received: May 17, 2012

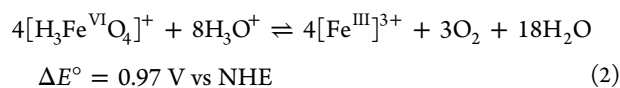
Published: August 19, 2012

with experiment.¹³ Though DFT approaches are frequently used to model energy landscapes of water oxidations,¹⁴ it is a challenge to corroborate the mechanisms proposed as well as to identify the formal oxidation state of the active catalyst.^{7–9,15} The present investigations highlight a structurally defined oxidant, known to undergo rapid exchange with aqueous solvent prior to stoichiometric production of O₂.^{10a}

The results obtained with ferrate have implications for oxygenic photosynthesis even though the overall spin states and coordination geometries of the reactive species differ.^{15,16} A high-resolution crystal structure of photosystem II (PSII) has been reported,¹⁷ along with spectroscopic studies^{18,19} that dissect the motions of protons and electrons needed to create the tyrosyl radical responsible for oxidizing the water-bound tetra-manganese/calcium cofactor, known as the oxygen-evolving complex (OEC) in PSII. In addition, isotopic studies have demonstrated that the OEC rapidly coordinates H₂O prior to O–O bond formation and release of O₂ with a favorable driving force.²⁰

It has been demonstrated that transition metal oxo complexes without unpaired d-electrons can behave in ways that resemble free oxygen radicals,²¹ which undergo O–O coupling reactions. This is possibly the result of accessible higher spin states, as observed for [Fe^{VI}O₄]^{2–}, which possesses a tetrahedral coordination geometry and d² electron configuration.^{22–24} Characterization in the solid state²³ and, here, in aqueous solution suggests that the monomeric ferrate resides in a triplet ground state. The ferryl unit is, therefore, similar to the isolated dangling manganyl proposed for the reactive (S₄) state in the OEC of PSII. In addition, the dimeric form of ferrate, referred to from this point on as diferrate, has a single μ-1,2-oxo bridge between iron centers, analogous to some structures proposed for S₄.^{15f,18e} Apparently, open-shell character and electrophilicity are similar for iron(VI) and manganese(V) oxo species, thus enabling O–O bond formation with similarly low barriers.²⁵

The highly oxidizing nature of K₂FeO₄ makes it of great practical importance. The compound is widely used for water purification²² and in rechargeable “superbatteries”, which are benign to the environment.²⁶ Despite its value as an oxidant, the aqueous reactivity of ferrate has received relatively limited attention.^{10a,27–30} The thermodynamics has been thoroughly investigated, however,^{22,24} under acidic conditions where Fe^{VI}O₄^{2–} + 8H⁺ + 3e[–] ⇌ Fe^{III} + 4H₂O (E° = 2.2 V vs NHE) and in alkaline media where Fe^{VI}O₄^{2–} + 4H₂O + 3e[–] ⇌ Fe^{III} + 8OH[–] (E° = 0.72 V vs NHE). Thus, ferrate solutions rapidly generate molecular oxygen from water in accord with eq 2. At pH 1.0, this reaction is believed to involve triprotonated ferrate, [H₃Fe^{VI}O₄]⁺, which undergoes spontaneous condensation and dimerization to afford μ-1,2-oxo-bridged diferrate, [H₄Fe^{VI}O₇]²⁺, prior to producing O₂, together with solvated iron(III). The latter product is expected to form upon disproportionation of iron(II)²⁹ and iron(IV) intermediates.³¹



Two types of O–O bond formation mechanisms are examined experimentally and computationally in this study involving diferrate as well as the monoferrate precursors. DFT calculations implicate the lowest energy oxo-coupling and water attack transition states shown in Figure 1.

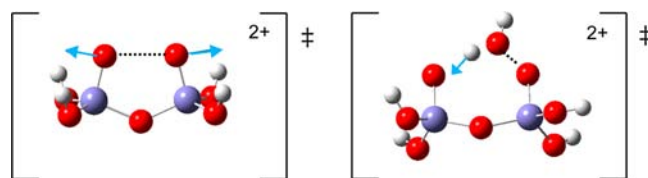


Figure 1. Oxo-coupling (left) and water attack (right) transition states accessed by the di-iron(VI)-containing [H₄Fe₂O₇]²⁺.

The transition states are associated with vibrational frequencies that can be used to compute ¹⁸O KIEs for comparison to experimental values determined using a competitive method and isotope ratio mass spectrometry (IRMS).^{11,13} This method is implemented under acidic conditions, where rapid exchange occurs between ferrate and ¹⁸O-labeled water.^{10a} The approach differs from monitoring isotope tracers, relying instead on the precise analysis of isotope ratios in the O₂ produced from natural abundance water.

The ¹⁸O KIEs are interpreted in view of the stopped-flow kinetics in H₂O and D₂O as well as the spectroscopic analysis of the intermediates and products formed. The most facile O₂ evolution pathway is proposed to involve a di-iron(VI) intermediate generated from K₂FeO₄. The experimental and computational findings regarding the propensity of diferrate to react by oxo-coupling versus water attack mechanisms are relevant to a proposed structurally and electronically related species in the OEC of PSII,^{15f,18e} as well as reactions proposed to involve synthetically derived iron(IV) and iron(V) oxidants.^{31c,32,33}

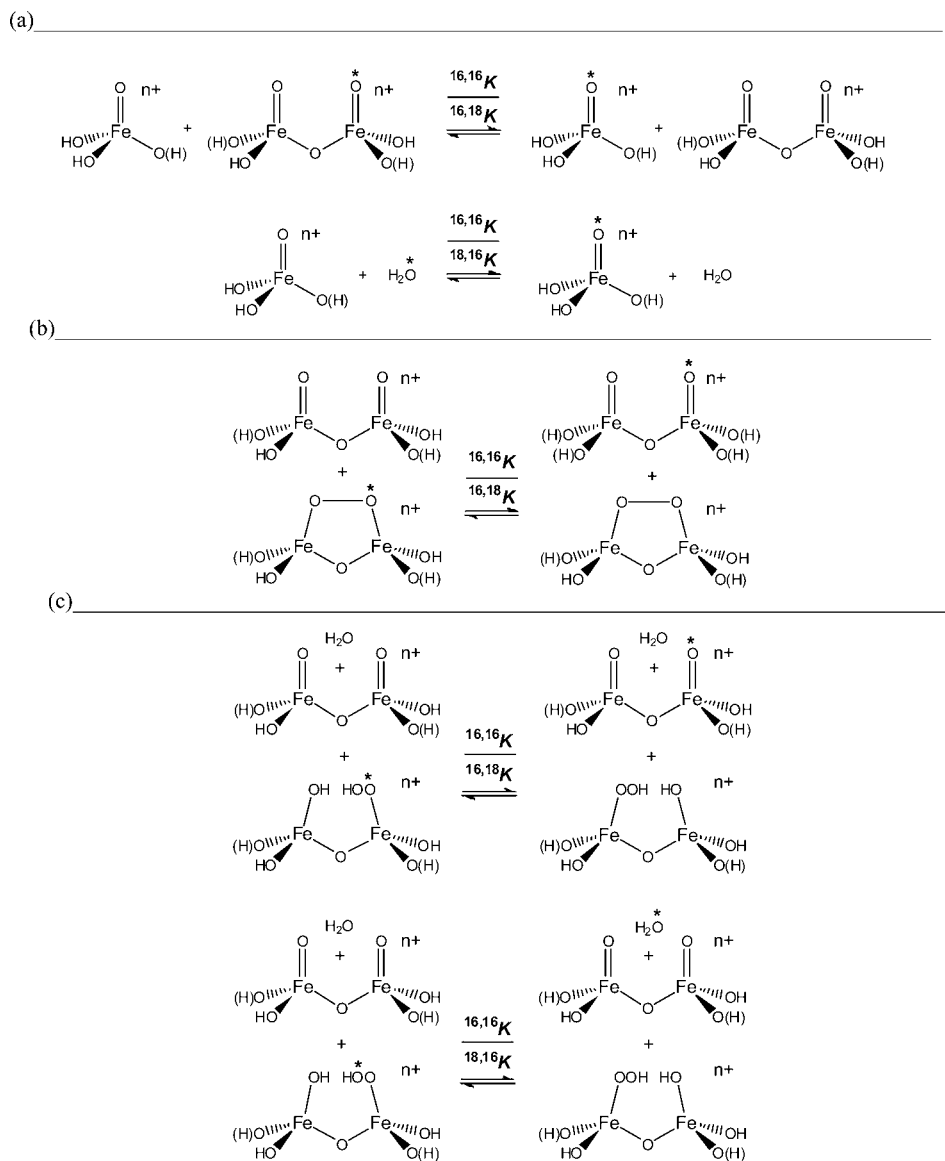
EXPERIMENTAL SECTION

1. Materials and Methods. K₂FeO₄ was either purchased from Sigma-Aldrich or synthesized following an established method.²⁷ Purity was assessed based on the electronic absorption spectrum of an aqueous solution using the extinction coefficient ε₅₁₀ = 1150 ± 20 M^{–1} cm^{–1}.^{27,29,30,33d} D₂O and DClO₄ were supplied by Cambridge Isotope Laboratories. Water of 18 MΩ resistivity was obtained using a Millipore ultrafiltration unit. Other reagent grade materials were from commercial sources and used without further purification.

All manipulations were carried out at a controlled temperature of 20 ± 2 °C unless noted. Electronic absorption in the UV–vis region was measured using a diode array (Agilent 8453) spectrophotometer or a rapid-mixing/rapid-scanning stopped-flow (OLIS RSM 1000). Electron paramagnetic resonance (EPR) spectra were acquired with an X-band (Bruker EMX) spectrometer operating at 9.47 GHz. A pH meter (Omega PHB-213) was used to prepare solutions of known acidity. The relationship pD = pH_{reading} + 0.4 was assumed for deuterated solutions.

Stopped-flow kinetic measurements, under a N₂ atmosphere, employed a pH/pD-jump procedure achieved by mixing equal volumes of aqueous K₂FeO₄ and ≤0.2 M HClO₄ or DClO₄ in the presence or absence of 5 mM potassium phosphate. Ionic strength was maintained at μ ≈ 0.1 M by adding NaClO₄. Buffer concentrations did not affect ferrate stability under the reaction conditions,^{29,30} as evidenced by the quantitative yields of O₂ observed. Solutions were prepared from dry samples of K₂FeO₄ (stored under N₂ in minimal light) and passed through a 0.22 μm PVDF filter (Millipore) before use. Data collected in the visible (400–620 nm) and ultraviolet (240–410 nm) ranges were analyzed by single value decomposition (SVD) as implemented by OLIS Globalworks and SPECFIT/32.³⁴ Monitoring the kinetics in the visible and UV spectral regions reveals differences in the time-dependent optical changes, which are corroborated by monitoring each reaction at fixed wavelengths of 510 or 335 nm.

EPR samples were prepared by manually mixing equal volumes of aqueous ferrate and H₂O or 0.2 M HClO₄ inside an EPR tube (Norell

Scheme 1. Isotope Exchange Equations Used in the Analysis of ^{18}O EIEs and ^{18}O KIEs, Where $n = 0, 1,$ or 2 Depending on Monomer and Dimer Protonation States^a

^aThe asterisk denotes the position of ^{18}O .

0.2 mm ID). After ~ 5 s, samples were immersed in acetone/ CO_2 (-78 °C) and then liquid N_2 (-196 °C). Spectra were recorded at 4 K using a liquid helium cryostat and externally referenced to a sample of the tri-*t*-butyl phenoxyl radical, which has a prominent absorption at 620 nm ($\epsilon_{620} = 400 \text{ M}^{-1} \text{ cm}^{-1}$) and a well established $g = 2.0045$.³⁵

Competitive ^{18}O KIEs were determined from the O_2 generated upon reacting ferrate with natural abundance H_2O . Samples of known pressures were analyzed by IRMS, as previously described.^{11–13} Multiple mixing procedures were utilized to initiate the reaction and ensure isotopic equilibration of the ferrate with H_2O on the time scale of O_2 production.^{10a} Typically, fixed volumes of He-saturated solutions (0.1 M HClO_4) were added to K_2FeO_4 (*in vacuo*). The black solid rapidly dissolved followed by a color change from violet to pale yellow. The O_2 evolved, measured by manometry, was consistently found to be $100 \pm 5\%$ of the yield expected, based on the initial concentration of K_2FeO_4 and the stoichiometry of eq 2.

After vacuum line purification, the O_2 produced upon exposure of ferrate to acidic aqueous solution was collected in a cold-trap containing 5 Å molecular sieves at -196 °C. The O_2 released from the sieves upon warming was completely combusted to CO_2 following

protocol.^{11,13} The CO_2 obtained is of identical isotope composition to the O_2 from which it was quantitatively produced. CO_2 pressures were analyzed using a capacitance manometer (Omega PX238). The gas was condensed into a dry glass tube, which was then flame-sealed for later IRMS analysis. Samples of CO_2 , containing the oxygen isotope composition of H_2O , were prepared using an established equilibration procedure.³⁶ All CO_2 samples were analyzed by IRMS to determine the $^{18}\text{O}/^{16}\text{O}$ to precisions of ± 0.2 parts per thousand (± 0.0002). The ratios of isotopes in O_2 and H_2O , designated R_{O_2} and $R_{\text{H}_2\text{O}}$, were analyzed using dual-inlet isotope ratio mass spectrometers at the University of Waterloo Environmental Isotope Laboratory and Johns Hopkins University Department of Earth and Planetary Sciences. The isotopic contents of all samples were reported relative to Vienna standard mean ocean water (VSMOW).³⁷

2. Density Functional Theory (DFT) Calculations. DFT calculations were performed using Gaussian 09W with the default grid.³⁸ Structures were optimized using the *mPW91* functional³⁹ and the following basis sets: 6-311G* (O), 6-31G (H), and CEP-31G (Fe).^{40,41} This protocol, designated BS-1, has been found to give vibrational frequencies that reproduce measured oxygen-18 equili-

rium isotope effects (^{18}O EIEs) over a wide range of temperatures.^{13b} The calculations in this study employed the same protocol to obtain vibrational frequencies of ferrate and diferrate, in various protonated ground states, as well as several transition states, defined by exactly one imaginary mode.

Single point free energy corrections (G_{corr}) were applied using the SMD density model and optimized gas-phase geometries.⁴² The difference between the gas phase electronic energy ($E_{\text{BS-1}}$) and the SMD electronic energy (E_{SMD}) is the free energy of solvation (ΔG_{SMD}) in eq 3. Solvated free energies (G_{sol}) were calculated for the geometries above using the *mPW91* functional and a larger basis set with diffuse functions (BS-2): 6-311++G** (O and H) and SDD (Fe) to afford $E_{\text{BS-2}}$.⁴³ The solvated free energy (G_{sol}) was calculated by substituting the results of eqs 3 and 4 into eq 5 where the gas phase free energy (G_{gas}) is equated to the sum of $E_{\text{BS-2}}$ and G_{corr} , adjusted by ΔG_{SMD}

$$E_{\text{SMD}} - E_{\text{BS-1}} = \Delta G_{\text{SMD}} \quad (3)$$

$$E_{\text{BS-2}} + G_{\text{corr}} = G_{\text{gas}} \quad (4)$$

$$G_{\text{gas}} + \Delta G_{\text{SMD}} = G_{\text{sol}} \quad (5)$$

Additional energy corrections to purify the assumed unrestricted singlet states of diferrate as well as the associated transition states of spin-contamination were undertaken using the method of Noodleman.⁴⁴ The results obtained were uniformly stabilizing by ≤ 3 kcal mol⁻¹. Because the corrections had no impact on any of the trends in this study, they appear entirely in the Supporting Information. Only uncorrected values are presented in the following text. The triplet state of monomeric ferrate was not corrected for spin contamination either, although a quintet excited state reported earlier⁴⁵ was located ca. 20 kcal mol⁻¹ higher in energy.

Multiple transition states for O–O bond formation within diferrate and ferrate were identified in the gas phase. These structures exhibit a single, mass-dependent imaginary frequency, which was used along with the stable vibrational modes to calculate oxygen-18 kinetic isotope effects (^{18}O KIEs). Transition states were corroborated by analyzing the intrinsic reaction coordinate (IRC) connecting the energy minima of the reactant and product states.⁴³ The structures obtained were reoptimized for analysis of Mulliken spin densities. All reaction pathways were, thus, mapped using the BS-1 protocol to apply the unrestricted Kohn–Sham (KS) formalism to open-shell species. Geometries optimized in the gas phase were subject to vibrational frequency analysis to verify stationary points and provide the necessary input.¹³ These vibrations were used without scaling or correction for anharmonicity.

3. Calculations of Isotope Effects. Oxygen-18 equilibrium isotope effects (^{18}O EIEs), defined by the ratio of isotopic equilibrium constants (e.g., $^{16,16}k/^{16,18}k$), were calculated from the vibrations of the reactant and product states using the approach of Bigeleisen and Goepfert-Mayer,⁴⁶ in accord with the Redlich–Teller Product Rule.⁴⁷ Isotope exchange reactions (e.g., $A + B^* \rightleftharpoons A^* + B$), with the asterisk denoting the site of ^{18}O , were formulated, and ^{18}O EIEs were calculated as the product of reduced partition function ratios (eq 6). These terms refer to isotope effects on the zero point energy (ZPE), the vibrational excitation energy (EXC) and the mass and moments of inertia (MMI).⁴⁸

$$^{18}\text{O EIE} = \text{ZPE} \times \text{EXC} \times \text{MMI} \quad (6)$$

^{18}O KIEs, defined by the ratio of rate constants leading to formation of the light O_2 in preference to the heavier isotopologue (e.g., $^{16,16}k/^{16,18}k$), were calculated within the context of transition state theory according to eq 7. Here terms include the isotope effect on the imaginary mode defining the reaction coordinate ($^{18}\nu_{\text{RC}}$) and the isotope effect on the pseudoequilibrium constant for attaining the transition state from the ground/intermediate state precursor(s) ($^{18}K_{\text{TS}}$). The $^{18}K_{\text{TS}}$ was calculated in the same manner as the ^{18}O EIE described above, as the product of the $\text{ZPE} \times \text{EXC} \times \text{VP}$. The VP signifies a vibrational product, defined by removing the one term from the MMI corresponding to the transition state and adding an imaginary mode to describe its “decomposition frequency”.

$$^{18}\text{O KIE} = ^{18}\nu_{\text{RC}} \times ^{18}K_{\text{TS}} \quad (7)$$

The isotope exchange reactions used in the analysis are given in Scheme 1. Equations 8 and 9 are needed for asymmetric reactions that possess an intramolecular isotope effect, albeit very small, in addition to the intermolecular one. Differences in the electronic and thermal free energies afforded the Boltzmann weighting factors (w_1 and w_2). Incidentally, weighting corrections were negligible when considering calculated isotope effects to the third decimal place, which is also the experimental limit.

$$^{18}\text{O EIE} = w_1 \left(\frac{^{16,16}K}{^{16,18}K} \right) + w_2 \left(\frac{^{16,16}K'}{^{18,16}K'} \right) \quad (8)$$

$$^{18}\text{O KIE} = w_1 \left(\frac{^{16,16}\nu_{\text{RC}} ^{16,16}K_{\text{TS}}}{^{16,18}\nu_{\text{RC}} ^{16,18}K_{\text{TS}}} \right) + w_2 \left(\frac{^{16,16}\nu_{\text{RC}} ^{16,16}K_{\text{TS}}}{^{18,16}\nu_{\text{RC}} ^{18,16}K_{\text{TS}}} \right) \quad (9)$$

RESULTS

1. Spectroscopic Characterization. K_2FeO_4 in aqueous solution is self-buffering to pH 9 and exhibits an electronic absorption spectrum with a prominent band at 510 nm (Figure 2). The addition of a small volume of concentrated HClO_4 to

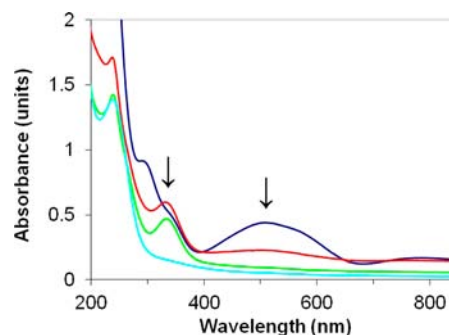


Figure 2. Spectra obtained upon acidifying aqueous K_2FeO_4 (0.43 mM) to pH 1 (0.1 M HClO_4).

bring the solution to pH 1.0 revealed the formation of a metastable intermediate with a diminished molar extinction coefficient ca. 500 nm.⁴⁹ A prominent feature at 335 nm is also observed on a longer time scale than bleaching in the visible region in Figure 2. This species was further characterized by stopped-flow experiments at variable concentrations of K_2FeO_4 .

The disappearance of the 335 nm species in Figure 2 was analyzed between 260 and 410 nm. The data obtained are inconsistent with those expected for the di-iron(VI) intermediate, which is found to decay within 50 ms when examined at wavelengths of 400–620 nm. The decay of the 335 nm species is much slower, occurring on the time scale of seconds. Thus, the optical changes correspond to a secondary reaction of a di-iron(III) or di-iron(IV) species. Di-iron(III) complexes⁵⁰ have been observed to undergo hydrolysis to $[\text{Fe}^{\text{III}}(\text{OH})_2]_2^{3+}$, which absorbs at 240 nm, on the observed time scale.^{51,52} In contrast, the di-iron(IV) complex expected to form upon release of O_2 into solution is likely to be obscured by rapid disproportionation, ultimately generating the iron(III) products observed in the freeze-trapping EPR experiments presented below.

Manual mixing was used to prepare samples analyzed by X-band EPR spectroscopy. These measurements are on the same time scale as electronic absorption spectra shown in Figure 2. An aqueous sample of K_2FeO_4 (0.48 mM) was compared with

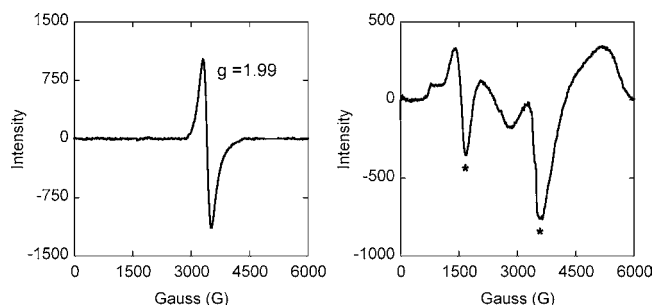


Figure 3. X-band EPR spectra (at 4 K) of frozen samples of K_2FeO_4 in aqueous solution (left) and after manual mixing with HClO_4 to obtain a solution of pH = 1.0 (right). The asterisks denote the expected positions of iron(III) signals.

a second sample of ferrate at the same concentration in 0.1 M HClO_4 . The EPR spectra shown in Figure 3 were acquired at 4 K with a 0.201 mW power, 20 G modulation amplitude, and 100 kHz modulation frequency. As shown in Figure 3, unreacted ferrate is characterized by a very broad isotropic signal at $g = 1.99$ (3406.5 G) with a peak to trough separation of 216.5 G.^{23b} The EPR spectrum obtained after dissolving ferrate in 0.1 M HClO_4 appears to contain at least two products, consistent with the $g = 4.3$ and $g = 2.0$ expected for high-spin and low-spin iron(III), respectively.⁵³

The EPR analysis in Figure 3 suggests products formed from di-iron(IV) or di-iron(III) complexes. This observation is consistent with decay of the 335 nm intermediate, initially observed in Figure 2 and found to occur with a ferrate-independent rate constant of $\sim 0.5 \text{ s}^{-1}$ by global analysis of

stopped-flow data collected in the UV region. These results point to breakdown of a di-iron(III) complex,^{50–52} rather than a di-iron(IV) complex, which is expected to form from the di-iron(VI) intermediate, together with O_2 on a shorter time scale.^{29,31,54,55} Added proof comes from the observation that $\text{Na}_4\text{Fe}^{\text{IV}}\text{O}_4$, prepared in the solid state, undergoes rapid disproportionation upon dissolving in H_2O to form iron(VI) and iron(III) products.⁵⁶

2. Kinetic Analysis. Stopped-flow experiments were conducted inside a N_2 -filled glovebox by mixing equal volumes of deoxygenated solutions containing K_2FeO_4 (~ 0.2 to 2.0 mM) and HClO_4 or DClO_4 ($\leq 0.2\text{M}$) at 20 °C. Some solutions contained 5 mM potassium phosphate, and the ionic strength was maintained at $\mu = 0.1 \text{ M}$ by addition of NaClO_4 . One electronic absorption spectrum was typically acquired every millisecond, following a 2–3 ms mixing time. Data were collected using the OLIS RSM1000 primarily in the 400 to 620 nm range, but also in the 240 to 410 nm range to observe a 335 nm intermediate. As in earlier studies, phosphate (5 mM) was added to chelate Fe^{III} at pH and pD values > 1.0 , thereby, avoiding the formation of colloidal iron oxides on the experimental time scale. Added phosphate can accelerate ferrate decomposition.^{29,30} Therefore, quantification of O_2 production was used to ensure that this reaction was negligible under the experimental conditions. Fitted time traces characteristic of optical changes in the visible region are shown in Figure 4 along with the initial and final calculated spectra.⁴⁸

It appears that the initial calculated spectra at pH 1.0 and pH 2.7 arise from optically distinct species; the former actually resembles the product formed from the latter. Supporting evidence for a common diferrate intermediate and the differing

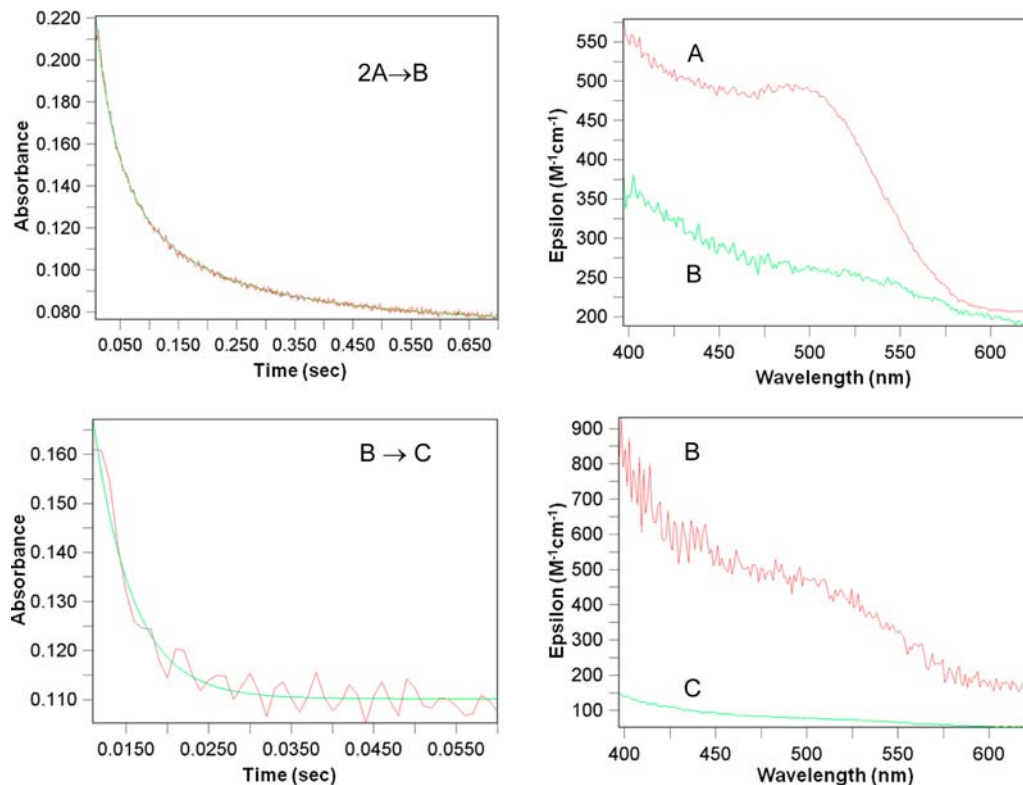


Figure 4. Time-dependent changes in absorbance at pH 2.7 (top), where data are shown fitted to a bimolecular decay, and at pH 1.0 (bottom), where data are fitted to a unimolecular decay. The calculated reactant (red) and product (green) spectra are based on the initial concentration of K_2FeO_4 .

reaction molecularity indicated by the fitting routines comes from experiments at variable K_2FeO_4 , where rates transition from concentration-dependent to concentration-independent.⁴⁸

The pronounced optical changes upon acidification of $[Fe^{VI}O_4]^{2-}$ have previously been used to assign pK_a values to three protonated forms.^{29,30} The initial calculated spectrum, extracted from global analysis of the stopped-flow data acquired at pH 2.7, exhibits a distinct band at 495 nm with $\epsilon_{495} \cong 500 \pm 20 \text{ M}^{-1} \text{ cm}^{-1}$. This result is consistent with earlier assignments of H_2FeO_4 and $[H_3FeO_4]^+$.^{29,30,33b-d} A linear variation of observed rate constant with initial K_2FeO_4 concentration can be resolved from pH 2.7 to 1.3.⁴⁸ This behavior is consistent with fitting of the time trace to a bimolecular decay $2A \rightarrow B$ and the reactivity of $[H_3FeO_4]^+$. Yet similar results were obtained when data were fitted to parallel unimolecular and bimolecular decay processes or to $2A \rightarrow B \rightarrow C$, leading to some ambiguity concerning the identity of the proposed di-iron(VI) intermediate and its visible absorption spectrum.

As the solution pH is decreased to 1.0, observed rate constants become independent of K_2FeO_4 concentration and an increased unimolecular decay component is evident. Under these conditions, rates are only fitted by a single exponential decay, referred to above as $B \rightarrow C$. The assignment of the initial spectrum to intermediate B, the product of the reaction at pH 2.7 (shown in Figure 4) may be an oversimplification, however, considering that the optical spectrum is difficult to define and the di-iron(VI) intermediate may exist in different protonation states.

The diferrate is expected to exist as $[H_4Fe_2O_7]^{2+}$ at the lowest pH examined.^{29,30} This intermediate is formulated with a single μ -1,2-oxo bridge between the iron(VI) centers, by analogy with dichromate. This structure is corroborated in the present experimental and computational studies. Under the most acidic conditions, $[H_4Fe_2O_7]^{2+}$ is believed to form within the time scale of rapid mixing (<3 ms) due to condensation and dimerization of ~85% of the ferrate, existing as $[H_3FeO_4]^+$, based on the reported $pK_a = 1.6 \pm 0.2$.²⁹ H_2FeO_4 is dominant at pH 2.7 due to the $pK_a = 3.5 \pm 0.2$.^{29,30}

Mixed order rate laws have been previously reported for water oxidation by acidic ferrate.²⁹ In addition, second-order rate constants spanning the acidic and alkaline regions have been approximated by a three pK_a model.³⁰ In this study, we focus upon the sensitivity of rate constant to solvent isotope in the acidic range exclusively. The results validate the interpretation of the transition from second-order to first-order kinetic behavior described above, in terms of rate-limiting steps involving ferrate and diferrate, respectively.⁴⁸ In addition, the presence of apparent inverse solvent kinetic isotope effects substantiate the predicted pK_a values and that $[H_3FeO_4]^+$ is more reactive than H_2FeO_4 .

Stopped-flow experiments probed the pH and pD dependences of observed rate constants. Apparent solvent deuterium kinetic isotope effects (D_2O KIEs) were analyzed using a single fitting protocol at the same acidity level in H_2O and D_2O . The presence of a normal D_2O KIE serves as a test for rate-limiting O–H(D) bond cleavage, as observed for certain water attack mechanisms⁵⁷ and expected for rate-limiting formation of an unbound hydroxyl radical or hydrogen peroxide intermediate. As mentioned, the kinetic profiles are complicated by the presence of a pK_a in the middle of the pH and pD ranges. At the lowest pH and pD examined, $[H_3FeO_4]^+$ and $[D_3FeO_4]^+$ are expected to form in nearly equal concentrations and react instantaneously to generate $[H_4Fe_2O_7]^{2+}$ and H_2O or

$[D_4Fe_2O_7]^{2+}$ and D_2O within the mixing time of the stopped-flow experiments. Under these conditions, the D_2O KIE is indistinguishable from unity. In less acidic solutions, inverse D_2O KIEs are observed due to the faster oxidation of D_2O than H_2O at the same pH and pD.

The D_2O KIE values, representing the ratio of apparent unimolecular and bimolecular rate constants, are quoted here with $\pm 2\sigma$ errors. An inverse D_2O KIE = 0.43 ± 0.09 is observed at pH and pD 2.7, whereas a negligible D_2O KIE = 0.95 ± 0.15 is observed at pH and pD 1.0. Disappearance of the inverse isotope effect coincides with disappearance of the second-order contribution to the kinetics, exposing the direct reactions of $[H_4Fe_2O_7]^{2+}$ and $[D_4Fe_2O_7]^{2+}$. Results depicting the pH and pD profiles of the bimolecular rate constant (k_{bi}), defined in the K_2FeO_4 concentration-dependent regime are summarized in Figure 5.⁴⁸ Theoretical curves for one state/one pK_a models,

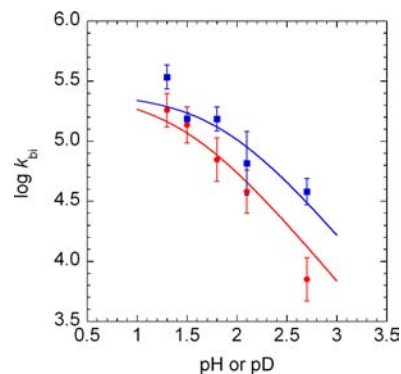


Figure 5. Computed bimolecular rate constant (k_{bi}) at varying pH (red circles) and pD (blue squares). The curves reflect the expression $\log k_{obs} = \log[k_{max}/(1 + 10^{pH-pK_a})]$ where $k_{max} = 2.5 \times 10^5 \text{ M}^{-1} \text{ s}^{-1}$ and $pK_a = 1.5$ (H_2O) or 1.9 (D_2O).

superimposed on the experimental results, indicate a maximum of $k_{bi} = 2.5 \times 10^5 \text{ M}^{-1} \text{ s}^{-1}$ and pK_a values of 1.5 in H_2O and 1.9 in D_2O . Including an additional pK_a had no impact on the results, nor did modeling improve upon considering additional reactive states.

3. Measurement of ^{18}O KIEs. Samples of O_2 were isolated upon dissolving varying quantities of K_2FeO_4 in aqueous acidic solutions. Because previous studies had shown that ^{18}O -labeled H_2O exchanges rapidly with ferrate under the experimental conditions,^{10a} competitive ^{18}O KIEs were determined from the ratio of $^{16,16}O_2$ to $^{16,18}O_2$ formed from natural abundance H_2O . Because of its very high concentration (~55.6 M), a change in the isotopic composition of H_2O is immeasurable upon treatment with K_2FeO_4 in 0.1 M $HClO_4$ and at higher pH where solutions contain $\leq 0.005 \text{ M}$ phosphate.

The determination of the competitive ^{18}O KIE was performed using IRMS to determine the $^{18}O/^{16}O$ in the O_2 evolved (R_{O_2}) relative to the $^{18}O/^{16}O$ of the unreacted H_2O (R_{H_2O}). $R_{H_2O} = 0.9940 \pm 0.0008$ vs SMOW was determined by analysis of multiple samples of pure H_2O and H_2O treated with $HClO_4$, K_2FeO_4 , or both. Due to the excess of water and rapid solvent exchange, the R_{H_2O} is the same as the ratio of isotopes in the ferrate initially present.

Multiple preparations of K_2FeO_4 were used in the competitive isotope fractionation experiments. Samples of O_2 were collected after the reaction of the solid K_2FeO_4 with a helium-saturated solution of 0.1 M $HClO_4$ or by introducing

the acid into aqueous ferrate solutions that had been pre-equilibrated for 2 to 12 h. Concentrations of K_2FeO_4 determined from absorbance readings at 510 nm, were compared with the pressures of CO_2 obtained after the production, isolation, and complete combustion of pure O_2 . Yields determined in this manner were $100 \pm 5\%$ based on eq 2 despite the purity of K_2FeO_4 , which varied from 35% to 99%.

In the analysis of oxygen isotope fractionation, H_2O may be treated as an “infinite reservoir”,⁵⁸ that is, its molar consumption is so small that changes in conversion can be neglected when estimating the ^{18}O KIE from $R_{\text{H}_2\text{O}}/R_{\text{O}_2}$ as indicated in eq 11. A more precise ^{18}O KIE is determined from fractional changes in the pressures of O_2 and linear regression to quantify the $^{18}\text{O}/^{16}\text{O}$ remaining in the H_2O (R_f) at varying fractional conversion (f). The R_f is calculated from the $R_{\text{H}_2\text{O}} = R_f(1-f) + R_{\text{O}_2}(f/2)$, where the $^{18}\text{O}/^{16}\text{O}$ in the H_2O is defined at $f = 0$ and the $f/2$ reflects the stoichiometry of O_2 produced per molecule of H_2O .

$$^{18}\text{O KIE} = \left[1 + \frac{\ln(R_f/R_0)}{\ln(1-f)} \right]^{-1} \cong \frac{R_{\text{H}_2\text{O}}}{R_{\text{O}_2}} \quad (11)$$

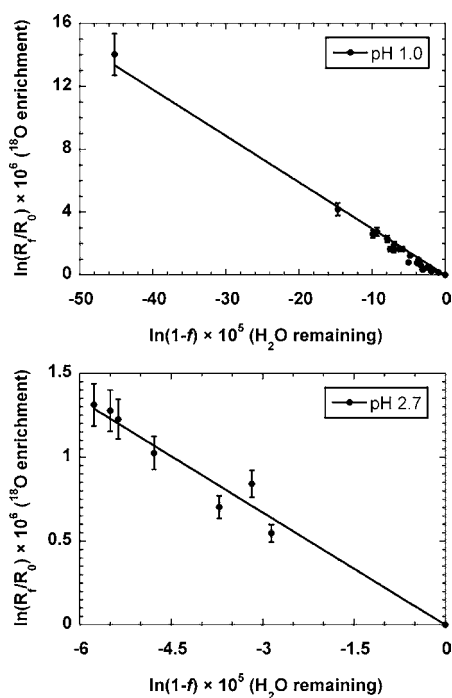


Figure 6. Isotopic fractionation by K_2FeO_4 at the pH values indicated; $\mu = 0.1$ M for solutions containing HClO_4 and phosphate (0–0.005 M). Errors are $\pm 1\sigma$ about the mean calculated value.

Figure 6 depicts the isotopic data fitted to eq 11. The slope resulting from the ^{18}O isotope enrichment in the remaining H_2O gives an ^{18}O KIE = 1.0303 ± 0.0014 . This value is somewhat larger than the $R_{\text{H}_2\text{O}}/R_{\text{O}_2} \cong 1.023 \pm 0.006$ at pH 1.0. The divergence is probably due to the large range in O_2 sample sizes. To be conservative, an average ^{18}O KIE = 1.027 ± 0.006 is quoted in the Discussion.

Measurements at pH 2.7 are also shown for comparison. These data were collected under conditions where $[\text{H}_3\text{FeO}_4]^+$ ($\text{p}K_a$ 1.6 ± 0.2) and H_2FeO_4 ($\text{p}K_a$ 3.5 ± 0.2) are both present,

and there is evidence for significant rate-limitation by dimerization, although the moderately large ^{18}O KIE is thought to be determined by a reaction downstream. Though fewer points were analyzed under these conditions, the ^{18}O KIE = 1.0229 ± 0.0007 derived from linear regression is indistinguishable from $R_{\text{H}_2\text{O}}/R_{\text{O}_2} \cong 1.022 \pm 0.004$, suggesting an average ^{18}O KIE at pH 2.7 that is somewhat smaller than that at pH 1.0.

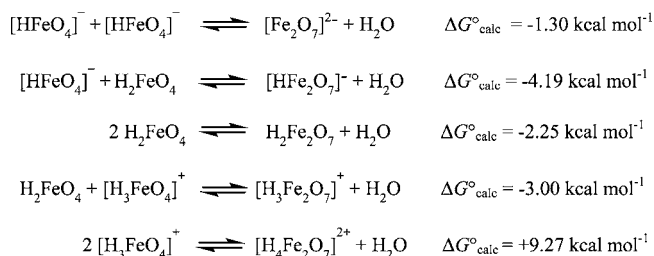
4. DFT Characterization of Ferrate and Diferrate Intermediates. The protonation of ferrate has been examined computationally and findings suggest a significant effect upon electronic structure with the α spin redistributing onto a single oxo ligand (3O). The Mulliken spin accumulates in the order $[\text{FeO}_4]^{2-} < [\text{HFeO}_4]^- < \text{H}_2\text{FeO}_4 < [\text{H}_3\text{FeO}_4]^+$, as summarized in Table 1 and depicted in Figure 7. At the same time, change in the unpaired spin on iron is much smaller.

Table 1. Mulliken Spin Densities for Different Protonation Levels of Ferrate in the Triplet Ground State

ferrate	1Fe	2O	3O	4O	5O
$[\text{FeO}_4]^{2-}$	1.27	0.18	0.18	0.18	0.18
$[\text{HFeO}_4]^-$	1.19	0.00	0.33	0.23	0.23
H_2FeO_4	1.20	0.06	0.54	0.11	0.06
$[\text{H}_3\text{FeO}_4]^+$	1.13	0.02	0.77	0.02	0.02

The extent of (α) spin buildup at a terminal oxo ligand correlates with the increased energy and reactivity of ferrate; however, the thermodynamics of condensation and dimerization ranges from slightly favorable to unfavorable upon increasing the level of protonation (Scheme 2). The lack of a

Scheme 2. Free Energies Calculated for the Formation of Diferrate at 293.15 K



discernible trend in $\Delta G_{\text{calc}}^\circ$ suggests competing influences on the stability of two ferrate equivalents relative to diferrate and H_2O . Five different protonation states of diferrate were considered in the analysis, but only the three highest protonation states, relevant under acidic conditions, are described in detail. These complexes are likely to be antiferromagnetically coupled through the μ -1,2-oxo bridge⁵⁰ and are treated as unrestricted (broken-symmetry, BS) singlet spin states. As noted in the Experimental Section, corrections for spin contamination led to $\Delta G_{\text{calc}}^\circ$ for diferrate formation that was uniformly reduced by ca. 3 kcal mol⁻¹.⁴⁸

The core structure of diferrate is believed to resemble pyrophosphate ($\text{P}_2\text{O}_7^{2-}$),⁵⁹ pyrosulfate ($\text{S}_2\text{O}_7^{2-}$),⁶⁰ and dichromate ($\text{Cr}_2\text{O}_7^{2-}$).⁶¹ Each of these compounds forms by acid-catalyzed condensation and dimerization of tetrahedral precursors to afford μ -1,2-oxo bridged structures, which undergo protonation at the oxygen ligands. Interestingly, this reaction sequence has been proposed to account for the exchange of oxygen-18 labeled H_2O with dichromic acid,⁶²

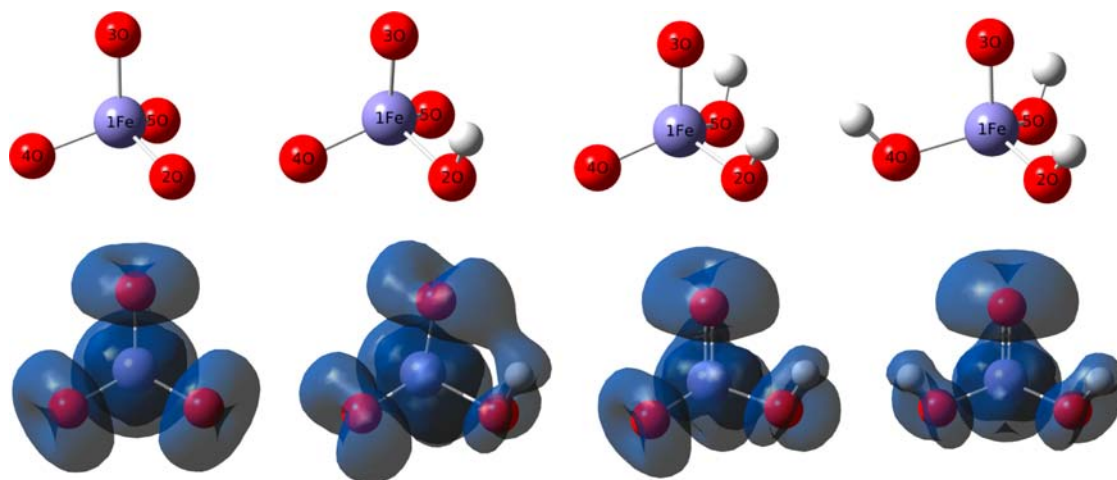


Figure 7. Calculated monomeric ferrate structures and α spin densities.

where $\Delta G^\circ = -18.8 \text{ kcal mol}^{-1}$.⁶³ The latter value is in line with the compound's stability with respect to O_2 release, even in strongly acid solution.

Under the experimental conditions, diferrate formation from ferrate appears to be rapid and reversible, prior to the evolution of O_2 per eq 2.^{29,30} ^{18}O EIEs corresponding to the reactions in Scheme 2 were calculated as outlined above in Scheme 1a. The production of $[\text{H}_4\text{Fe}_2\text{O}_7]^{2+}$ is characterized by an ^{18}O EIE = 1.0023 and values of comparable magnitude are calculated for $[\text{H}_3\text{Fe}_2\text{O}_7]^+$ and $\text{H}_2\text{Fe}_2\text{O}_7$. These ^{18}O EIEs are an order of magnitude smaller than the ^{18}O KIEs determined experimentally. As demonstrated below, these large normal ^{18}O KIEs are characteristic of irreversible O–O bond formation.

5. DFT Analysis of O–O Bond Formation. A. Diferrate.

To avoid potential issues related to changes in spin state, calculations were performed by treating reactions of diferrate along an unrestricted singlet energy surface. Saddle-point structures were identified and corroborated by IRC analysis before use in the ^{18}O KIEs calculations, which employ the Bigeleisen–Wolfsberg approach derived from transition state theory (cf. eq 7).^{47,64} Although a small amount of spin contamination is indicated in the reactant, product, and intervening transition state (TS),⁴⁴ associated energy corrections suggest uniform stabilization by a few kilocalories per mole at most.⁴⁸ Due to the small sizes and inherent uncertainty of these corrections, unadjusted free energies are presented below, while spin-purified values are provided in the Supporting Information. Single-point free energy corrections were applied to account for solvation, using the SMD model in Gaussian09.^{42,43} In cases where multiple conformations of protonated diferrate exist, the calculations correspond to those with the lowest energies.

In the following tables, diferrate reaction pathways are designated according to spin state, protonation level, and mechanism of O–O bond formation. For example, the TS for oxo-coupling (OC) within the tetraprotonated dimer, $[\text{H}_4\text{Fe}_2\text{O}_7]^{2+}$, via the unrestricted singlet state is designated ^1_4OC . The same nomenclature applies to water attack (WA), except that an additional designation is needed for asymmetric species, for example, $[\text{H}_3\text{Fe}_2\text{O}_7]^+$ and $[\text{HFe}_2\text{O}_7]^-$, which can react by at least two different pathways. Pathway WA1 involves O–O bond formation upon attack of a protonated oxo group at the same time an unprotonated oxo accepts the water O–H. In the WA2 pathway, the converse occurs, and the O–O bond is

formed at an unprotonated oxo ligand, while a protonated oxo assists in cleaving the O–H bond.

Activation barriers and thermodynamic barriers are given as $\Delta G_{\text{calc}}^\ddagger$ and $\Delta G_{\text{calc}}^\circ$ in Table 2 for the OC and WA mechanisms

Table 2. Calculated Free Energy Barriers (in kcal mol^{-1}) for O–O Bond Formation within Diferrate

diferrate	$\Delta G_{\text{calc}}^\ddagger$	$\Delta G_{\text{calc}}^\circ$	diferrate	$\Delta G_{\text{calc}}^\ddagger$	$\Delta G_{\text{calc}}^\circ$
^1_4OC	4.27	−8.53	^1_2WA	27.82	17.73
^1_4WA	12.40	−6.82	^1_1OC	8.26	3.49
^1_3OC	6.22	−6.40	$^1_1\text{WA1}$	30.98	26.08
$^1_3\text{WA1}$	20.73	9.18	$^1_1\text{WA2}$	28.65	26.95
$^1_3\text{WA2}$	22.14	14.52	^1_0OC	10.09	8.87
^1_2OC	6.67	−0.80	^1_0WA	36.31	27.92

possible for all diferrate protonation states. Though the negatively charged diferrates do not exist under acidic conditions, they are included for purposes of comparison. Proceeding from left to right across the table, the protonation level decreases and $\Delta G_{\text{calc}}^\circ$ for O–O bond formation becomes less favorable. Further, the calculations predict that, for all forms of diferrate, OC is kinetically favored over WA by >6 kcal mol^{-1} . Overall, the $\Delta G_{\text{calc}}^\ddagger$ range, approximately, from 4 to 40 kcal mol^{-1} for reactions with $\Delta G_{\text{calc}}^\circ$ of −9 to 30 kcal mol^{-1} .

IRC calculations corroborate the TS structures for the OC and WA mechanisms of diferrate. Mulliken spin density analysis indicates that protonation of ferrate fragments cause accumulation of unpaired spin at the two reactive oxo positions of each tetrahedral fragment in the di-iron(VI) intermediate suggesting a state that appears to involve the coupling of two iron(V) oxyl radical centers. The lowest energy oxo-coupling TS is depicted in Figure 8. In this reaction, the highest energy α and β orbitals appear to be mirror images of one another, where via a TS with effective C_{2v} symmetry, spins localized on oxygen couple to form a bond. Table 3 summarizes how the spins on O3 and O7 of the reactant dissipate in the TS and vanish as the μ -1,2-peroxo bond is formed. The effect is more obvious beginning with the symmetric $[\text{H}_4\text{Fe}_2\text{O}_7]^{2+}$ and $\text{H}_2\text{Fe}_2\text{O}_7$ than the asymmetric $[\text{H}_3\text{Fe}_2\text{O}_7]^+$.

The TS for water attack upon $[\text{H}_4\text{Fe}_2\text{O}_7]^{2+}$ is depicted in Figure 9. Here, O14 of the preassociated water molecule attacks O3, concomitant with transfer of H14b to O7. This reaction can be described in molecular orbital terms as involving the

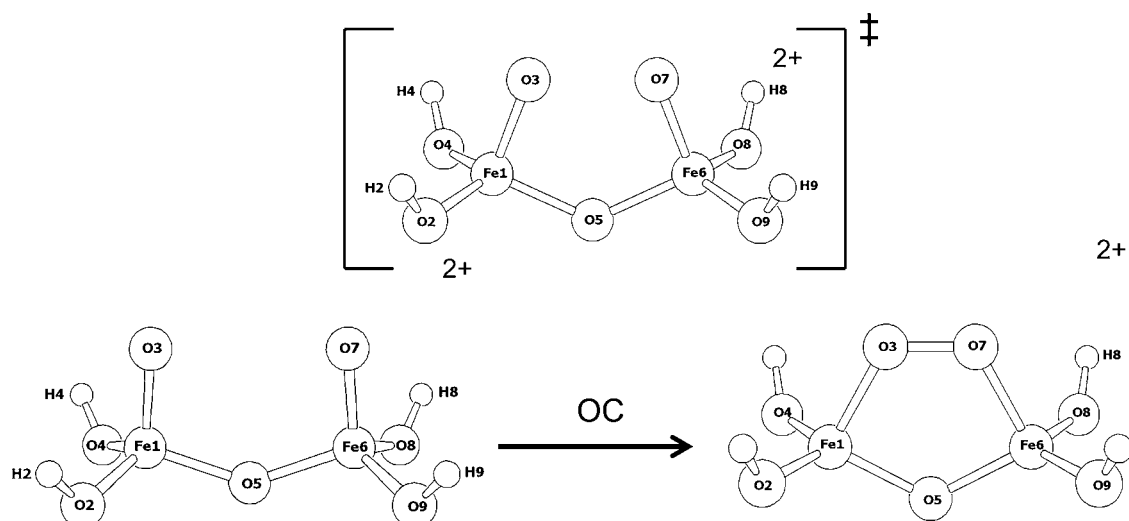


Figure 8. Intramolecular oxo-coupling (OC) in the TS identified for $[\text{H}_4\text{Fe}_2\text{O}_7]^{2+}$.

Table 3. Mulliken Spin Redistribution in the Reactant (R), Product (P), and Transition State (TS) of Oxo-Coupling (OC) Reactions of $[\text{H}_4\text{Fe}_2\text{O}_7]^{2+}$, $[\text{H}_3\text{Fe}_2\text{O}_7]^+$, and $\text{H}_2\text{Fe}_2\text{O}_7$

diferrate	Fe1	O2	O3	O4	O5	Fe6	O7	O8	O9
14_R	0.99	0.03	0.78	0.03	0.00	-0.99	-0.78	-0.03	-0.03
$^14_{TS}$	0.92	-0.02	0.62	-0.02	0.00	-0.92	-0.62	0.02	0.02
14_P	0.86	-0.01	0.12	-0.01	0.00	-0.86	-0.12	0.01	0.01
13_R	0.99	0.08	0.54	0.21	-0.05	-0.99	-0.72	-0.01	-0.02
$^13_{TS}$	0.97	0.06	0.27	0.13	-0.01	-0.77	-0.65	0.02	0.00
13_P	0.73	0.25	-0.17	0.00	0.00	-0.52	-0.28	0.00	0.00
12_R	1.10	0.10	0.52	0.09	0.00	-1.08	-0.44	-0.19	-0.11
$^12_{TS}$	0.92	0.07	0.38	0.07	0.00	-0.92	-0.38	-0.07	-0.07
12_P	0.79	0.17	0.05	0.03	0.00	-0.79	-0.05	-0.03	-0.17

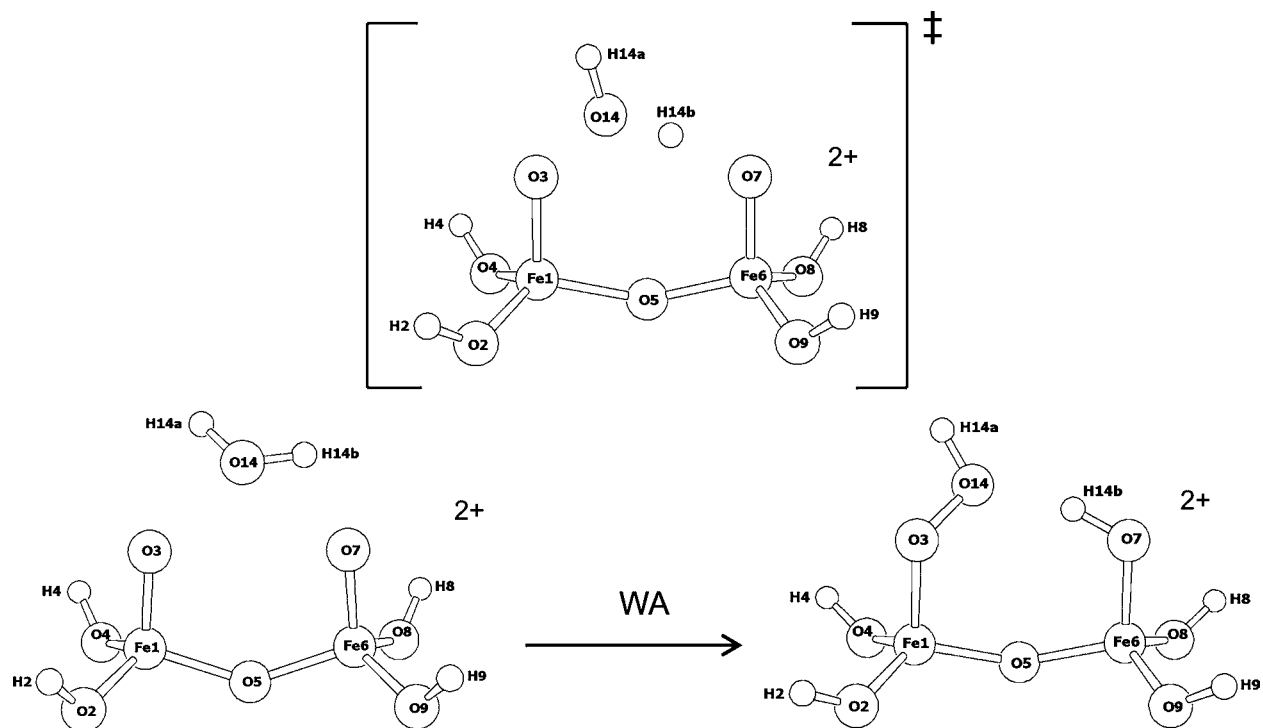


Figure 9. Water attack (WA) in the TS identified for $[\text{H}_4\text{Fe}_2\text{O}_7]^{2+}$.

Table 4. Mulliken Spin Redistribution in the Reactant (R), Product (P), and Transition State (TS) Associated with Water Attack (WA) upon $[\text{H}_4\text{Fe}_2\text{O}_7]^{2+}$ along an Unrestricted Singlet Energy Surface

diferrate	Fe1	O2	O3	O4	O5	Fe6	O7	O8	O9	O14	H14a	H14b
14_R	1.69	0.18	-0.02	-0.02	-0.04	-1.08	-0.24	-0.11	-0.16	-0.31	0.01	0.01
$^14_{TS}$	1.63	0.08	0.02	0.10	0.00	-1.37	-0.49	0.01	0.05	0.03	0.00	0.00
14_P	2.94	0.22	-0.42	0.23	-0.09	-2.15	-0.12	-0.16	-0.06	-0.39	0.01	-0.01

Table 5. Free Energy Barriers (in kcal mol⁻¹) to Oxo-Coupling (OC) and Water Attack (WA) Calculated for Tri- and Diprotonated Forms of Ferrate

Ferrate	$^33_{OC}$	$^32_{OC}$	$^33_{WA}$	$^32_{WA}$
$\Delta G^{\ddagger}_{calc}$	24.5	41.0	20.8	30.2
ΔG^p_{calc}	11.7	24.2	7.6	27.7

Table 6. Computed Gas Phase ^{18}O KIEs upon O–O Bond Formation by Protonated Diferrates

diferrate	^{18}O KIE _{calc} (^{18}O EIE _{calc})	$^{18}\nu_{RC}$	$^{18}K_{TS}$	ZPE (ZPE)	EXC (EXC)	VP (MMI)	$^{16,16}\nu_{RC}$ (cm ⁻¹)
$^14_{OC}^a$	1.0308 (0.9836)	1.0249	1.0058	1.0030 (0.9558)	1.0238 (1.0242)	0.9794 (1.0048)	209.21i
$^13_{OC}$	1.0302 (0.9884)	1.0233	1.0067	1.0056 (0.9653)	1.0450 (1.0428)	0.9356 (0.9595)	169.05i
$^12_{OC}$	1.0344 (0.9972)	1.0255	1.0086	1.0060 (0.9740)	1.0119 (1.0061)	0.9908 (1.0176)	192.80i
$^14_{WA}^a$	1.0147 (0.9851)	1.0175	0.9975	0.9659 (0.9601)	0.9775 (0.9652)	1.0523 (1.0597)	486.39i
$^13_{WA1}$	1.0076 (0.9902)	1.0080	0.9996	0.9633 (0.9520)	0.9191 (0.9134)	1.1282 (1.1383)	895.34i
$^13_{WA2}$	1.0044 (0.9900)	1.0067	0.9977	0.9585 (0.9529)	1.0628 (1.0542)	0.9586 (0.9639)	971.72i

^aA single imaginary mode was present in the gas phase $[\text{H}_4\text{Fe}_2\text{O}_7]^{2+}$ structure. The isotope shift of this low-frequency mode was, therefore, neglected in the calculations. If the contribution of this isotopic shift were significant, the ^{18}O KIEs would be slightly diminished. Isotope effects for all diferrate protonation states are provided in the Supporting Information.

Table 7. Computed Gas Phase ^{18}O KIEs upon O–O Bond Formation by Protonated Forms of Ferrate

ferrate	^{18}O KIE _{calc} (^{18}O EIE _{calc})	$^{18}\nu_{RC}$	$^{18}K_{TS}$	ZPE (ZPE)	EXC (EXC)	VP (MMI)	$^{16,16}\nu_{RC}$ (cm ⁻¹)
$^33_{OC}$	1.0456 (1.0001)	1.0261	1.0190	1.0404 (1.0051)	1.0020 (0.9890)	0.9773 (1.0058)	362.39i
$^32_{OC}$	1.0565 (1.0077)	1.0262	1.0295	1.0561 (1.0103)	0.9933 (0.9942)	0.9814 (1.0032)	633.17i
$^33_{WA}$	1.0019 (0.9909)	1.0034	0.9985	0.9630 (0.9560)	0.9768 (0.9712)	1.0600 (1.0658)	1058.89i
$^32_{WA}$	1.0123 (1.0070)	1.0077	1.0045	0.9758 (0.9737)	0.9747 (0.9700)	1.0552 (1.0649)	680.46i

addition of $\bullet\text{OH}$ and $\bullet\text{H}$, concertedly, to each open-shell ferryl, as opposed the electrons moving together concomitant with proton transfer. The Mulliken spin analysis in Table 4 suggests significant polarization within the H_2O -bound precursor, with spin density from one tetrahedral iron center evenly redistributed over the surrounding oxo ligands. Upon water attack, spin appears transmitted from O14 to the reactive ferryl ($\text{Fe1}=\text{O3}$). In the di-iron(V) product, electron density has fully transferred to each iron center with some spin at the proximal (O3) and terminal (O14) nuclei of the end-on (η^1)-coordinated hydroperoxo ligand.

B. Monomeric Ferrate. Multiple transition states with unattainably high barriers were located for O–O bond forming reactions of monomeric ferrate in its various states. The triprotonated and diprotonated forms relevant under the reaction conditions are highlighted, where calculations indicate triplet ground states lying ca. 20 kcal mol⁻¹ below a quintet excited state.⁶³ The description of K_2FeO_4 as a ground state

triplet ($S = 3$) is consistent with its magnetic properties in the solid state and frozen solution, as described here.²³

Hypothetical oxo-coupling and water attack mechanisms were evaluated for ferrate. The results compiled in Table 5 indicate that O–O bond formation is more favorable within $[\text{H}_3\text{FeO}_4]^+$ than H_2FeO_4 . The overall range of $\Delta G^{\ddagger}_{calc}$ is from 20 to 40 kcal mol⁻¹, with reactions of $[\text{H}_3\text{FeO}_4]^+$ thermodynamically favored in both cases. Apparently, oxo-coupling has a higher energy TS when two unprotonated oxo ligands react ($^32_{OC}$)⁶⁵ than when one protonated oxo reacts with an unprotonated oxo ligand ($^33_{OC}$). The water attack TS is also higher in energy for O–O bond formation involving an unprotonated oxo ligand, concomitant with proton/hydrogen atom transfer to a second unprotonated oxo ($^32_{WA}$), than the related reaction in which a protonated oxo ligand accepts the proton/hydrogen atom equivalent ($^33_{WA}$).⁶⁶

6. Predicted Oxygen-18 Isotope Effects. Reactant, TS, and product structures optimized in the gas phase were used to

extract vibrational frequencies for ^{18}O KIE and ^{18}O EIE calculations.^{13,48,64,67} Use of these vibrations in lieu of those derived from structures optimized in the aqueous dielectric continuum had a negligible impact.^{13,44c,64}

Only the protonated forms of diferrate and ferrate expected under acidic conditions are shown in Tables 6 and 7 to illustrate how the ^{18}O KIEs distinguish oxo-coupling from water attack.⁴⁸ The $\Delta G_{\text{calc}}^{\ddagger}$ (4–7 kcal mol⁻¹) are all similarly small for oxo-coupling within diferrate. Though the barrier increases slightly with decreasing protonation level for $[\text{H}_4\text{Fe}_2\text{O}_7]^{2+}$, $[\text{H}_3\text{Fe}_2\text{O}_7]^+$, and $\text{H}_2\text{Fe}_2\text{O}_7$, all ^{18}O KIE_{calc} fall within a narrow range (1.0302–1.0344), in agreement with the experimental value of 1.027 ± 0.006 . With respect to eq 7, the effects originate from a minor contribution from $^{18}K_{\text{TS}}$ (1.0058–1.0086) and a major contribution from $^{18}\nu_{\text{RC}}$ (1.0249–1.0255). The latter term, reflecting the mass dependence of the reaction coordinate frequency, is most likely the greatest source of error in the ^{18}O KIE calculations. A deviation of ± 1 cm⁻¹ in $^{18}\nu_{\text{RC}}$ results in a ± 0.005 change in the computed isotope effect;^{44c,64} this is comparable to the error in calculated and measured ^{18}O EIEs.¹³

The lowest energy barrier for water attack at a deprotonated oxo group is calculated to be ~ 12 kcal mol⁻¹ within an encounter complex of diferrate; that is, H_2O and $[\text{H}_4\text{Fe}_2\text{O}_7]^{2+}$. The TS is located lower in energy than all others derived for different diferrate protonation states; yet it is significantly higher than all TSs identified for oxo-coupling. The associated ^{18}O KIE_{calc} = 1.0147 is a maximum for this type of reaction, yet significantly smaller than the experimental value quoted above. While it is relatively easy to explain isotope effects smaller than predicted due to possible partial rate-limitation, it is more difficult (if not impossible) to explain larger than predicted isotope effects. The ^{18}O KIE_{calc} for water attack upon $[\text{H}_4\text{Fe}_2\text{O}_7]^{2+}$ arises from a small inverse $^{18}K_{\text{TS}}$ (0.9975) and a moderately sized normal $^{18}\nu_{\text{RC}}$ (1.0175). As diferrate is deprotonated, the WA barrier increases above 20 kcal mol⁻¹; in the process, the ^{18}O KIE_{calc} becomes 2–3 times smaller but does not follow a monotonic trend.^{48,68}

The $\Delta G_{\text{calc}}^{\ddagger}$ for O–O bond formation within the relevant protonation states of monomeric ferrate, $[\text{H}_3\text{FeO}_4]^+$ and H_2FeO_4 , range from 21 to 41 kcal mol⁻¹. These barriers, computed along triplet energy surfaces, are considerably larger than most barriers associated with diferrate, consistent with interpretations of the kinetics. The experimental ^{18}O KIE is overestimated by the significantly larger ^{18}O KIE_{calc} for oxo-coupling within ferrate, while the ^{18}O KIE_{calc} for water attack is significantly smaller.

DISCUSSION

1. Ferrate Reduction/Water Oxidation. Experimental and computational studies presented here suggest a pathway for ferrate-mediated water oxidation that involves rapid condensation and dimerization of a monomeric protonated iron(VI) starting material to form a metastable μ -1,2-oxo di-iron(VI) intermediate prior to intramolecular oxo-coupling. A di-iron(V) peroxide species is expected to form transiently, producing O_2 and the aquated di-iron(IV) product in the first irreversible step. This di-iron(IV) species is not expected to oxidize water on the experimental time scale^{31c} but instead to react by disproportionation to form iron(II) and iron(VI) or iron(III) and iron(V). The latter reaction is expected to be highly unfavorable,^{33,56} yet it is considered in Scheme 3 among the

mechanisms that can explain the reaction, which ultimately affords O_2 and the iron(III) products detected spectroscopically following ferrate-mediated water oxidation.

While single electron transfers are typically less challenging than multielectron transfers, this may not be true for disproportionation of the di-iron(IV) product in Scheme 3a. The reaction requires bringing together two dipositive charges and formation of a di-iron(V) intermediate, which is expected to be of much higher in energy than the di-iron(VI) starting material.^{29,33} A two-electron intramolecular heterolysis is, therefore, proposed in Scheme 3b.^{33d} Here, fragmentation of the di-iron(IV) intermediate at the μ -1,2-oxo bridge regenerates iron(VI) while producing the iron(II) detected in trapping experiments.⁵⁵ This is the simplest explanation that makes the fewest assumptions and allows all three O_2 equivalents to be formed by the same mechanism. It is impossible, however, to exclude the reaction in Scheme 3c, where one O_2 equivalent forms by an alternative route involving the high-energy iron(V) intermediate.

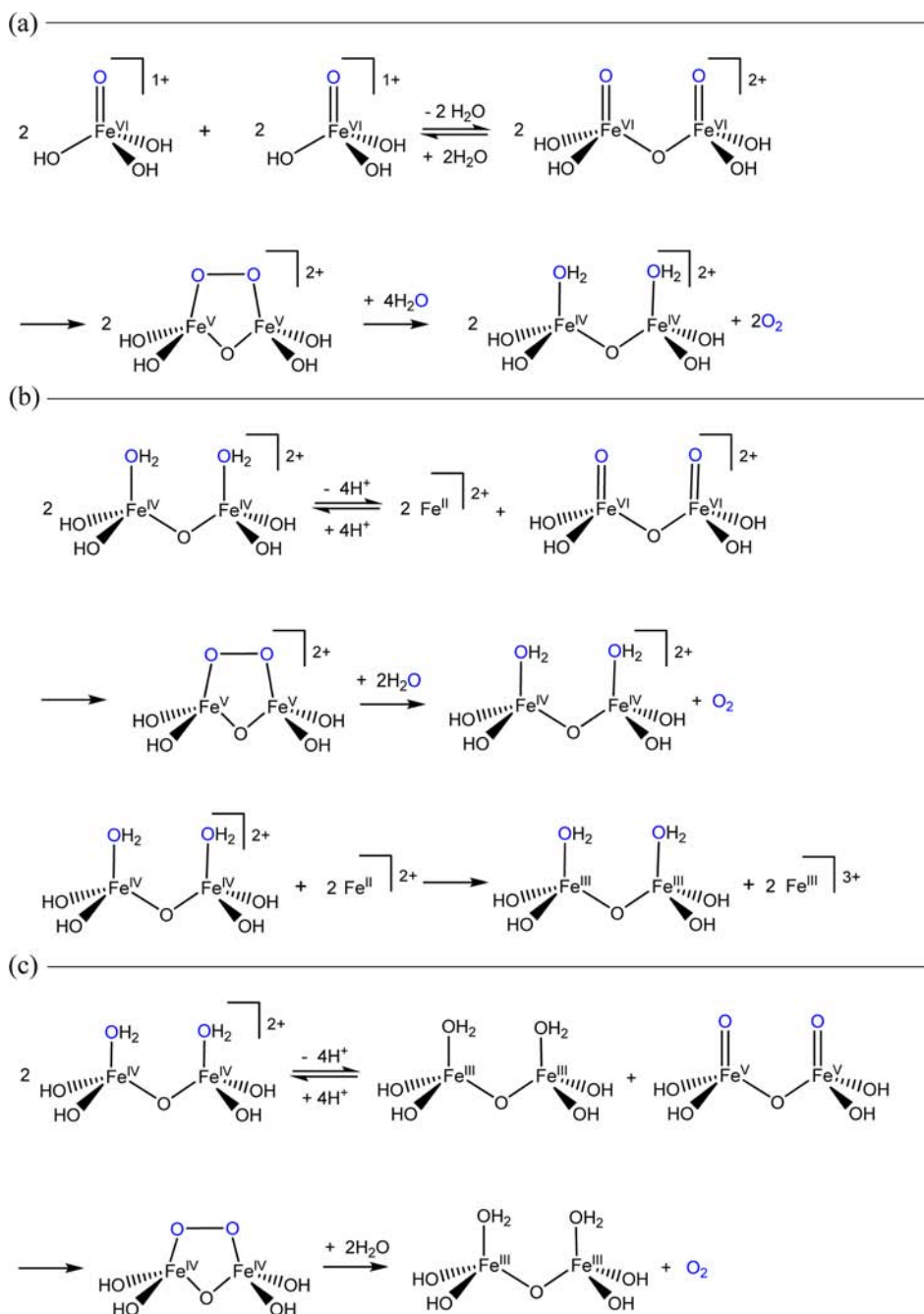
2. Analysis of the Kinetic Mechanism. Past studies have appreciated the complexity of ferrate-mediated water oxidation in acidic media and the possibility that two or more steps contribute to rate limitation.²⁹ In the present investigation, measurements were performed in H_2O and D_2O at varying acidities to understand the reaction kinetics.

The fastest measurable reaction occurs at pH and pD 1.0 where diferrate formation appears to occur within the mixing time of stopped flow experiments. This species disappears by a simple first-order decay, which is corroborated by the K_2FeO_4 concentration independence of observed rate constants derived from data collected in the visible region of the absorption spectrum.⁴⁸ Under these conditions, a slower secondary reaction is observed in the UV region, corresponding to disappearance of a 335 nm intermediate. The reaction is tentatively assigned to hydrolysis by a di-iron(III) complex. The analogous di-iron(IV) complex is expected to form $>10^2$ times faster, essentially at the same time O_2 is evolved from the di-iron(VI) starting material.

The transition from first-order to second-order kinetics as the solution acidity is decreased signals rate-limiting condensation and dimerization of ferrate, which is consistent with the increased sensitivity of rates to K_2FeO_4 concentration.⁴⁸ Under these conditions, time traces can be fitted to multiple decay functions. The $2\text{A} \rightarrow \text{B}$ description is favored because it does not constrain the calculated optical spectrum of the intermediate, B, nor does it amplify the pH and pD sensitivity of unimolecular rate constants. Such behavior would only be expected if rapid and reversible diferrate formation occurred prior to O–O bond formation.

The appearance of inverse solvent isotope effects as the solution pH and pD is raised corroborates the interpretation of the kinetics. At pH and pD 1.0, ^{18}O KIE = 0.95 ± 0.15 is derived from k_{uni} and at pH and pD 2.7, ^{18}O KIE = 0.43 ± 0.09 is derived from k_{bi} . Fitting k_{bi} at pH and pD as low as 1.3 to the 1 state/1 pK_a model in Figure 5 demonstrates that the change in solvent isotope effect is expected due to the ~ 0.4 unit increase in the pK_a of $[\text{D}_3\text{FeO}_4]^+$ in D_2O relative to $[\text{H}_3\text{FeO}_4]^+$ in H_2O .

The steady-state expression in eq 12 describes conversion of ferrate to diferrate followed by O–O bond formation in the rate-limiting step. Terms include k_1 and k_{-1} for the forward and reverse rate constants for converting two equivalents of $[\text{H}_3\text{FeO}_4]^+$ into $[\text{H}_4\text{Fe}_2\text{O}_7]^{2+}$ and H_2O as well as k_2 corresponding to the microscopic rate constant for O–O

Scheme 3. Proposed Mechanisms of O₂ Evolution by Diferrate under Acidic Conditions^a

^aTwo equivalents of O₂ are accounted for in mechanism a, while the third equivalent of O₂ arises from mechanism b or c.

bond formation. Aside from the proposed di-iron(VI) species, all other intermediates seem to be consumed faster than they are formed preventing accumulation to a detectable level.

$$\frac{-d[\text{K}_2\text{FeO}_4]}{dt} = \frac{k_1 k_2}{k_{-1}[\text{H}_2\text{O}] + k_2} \{[\text{H}_3\text{FeO}_4]^+\}^2 \quad (12)$$

Although multiple fitting procedures could be used to fit the time-dependent optical changes, experiments at variable ferrate concentrations suggest two distinct kinetic behaviors.⁴⁸ Considering eq 12 in the limit where $k_2 \gg k_{-1}[\text{H}_2\text{O}]$, the rate of ferrate disappearance approaches $(k_1)([\text{H}_3\text{FeO}_4]^+)^2$. In contrast, when $k_{-1}[\text{H}_2\text{O}] \gg k_2$, the rate approaches $(k_1 k_2 / k_{-1}[\text{H}_2\text{O}])([\text{H}_3\text{FeO}_4]^+)^2$. Substituting $[\text{H}_4\text{Fe}_2\text{O}_7]^{2+}$ for $(k_1 /$

$k_{-1}[\text{H}_2\text{O}])([\text{H}_3\text{FeO}_4]^+)^2$ gives eq 13, which represents the maximum unimolecular rate constant at pH and pD 1.0 and under less acidic conditions at sufficiently high concentrations of K₂FeO₄.⁴⁸ The expression does not include steps downstream of O–O bond formation because no evidence has been obtained for additional contributions. For instance, the dissociation of O₂ is predicted to exhibit an ¹⁸O KIE ≤ 1,¹³ inconsistent with the observation that the DFT-derived ¹⁸O KIE_{calc} ≈ 1.031 is comparable to the measured ¹⁸O KIE = 1.027 ± 0.006.

$$\frac{-d[\text{K}_2\text{FeO}_4]}{dt} = k_2[\text{H}_4\text{Fe}_2\text{O}_7^{2+}] \quad (13)$$

3. Predicted Energy Barriers and Isotope Effects. The kinetics in this study suggests that diferrate undergoes rate-limiting O–O bond formation. Although it is never possible to exclude the presence of a high-energy intermediate, the $k_{\text{uni}} = 185 \pm 23 \text{ s}^{-1}$ is computed by averaging ferrate-independent rate constants determined at pH and pD 1.0. The corresponding $\Delta G^\ddagger \cong 14 \text{ kcal mol}^{-1}$ represents the maximum activation energy in the adiabatic limit.^{69,70}

DFT calculations that predict a $\Delta G_{\text{calc}}^\circ \cong 9 \text{ kcal mol}^{-1}$ for the conversion of 2 equiv of $[\text{H}_3\text{FeO}_4]^+$ to $[\text{H}_4\text{Fe}_2\text{O}_7]^{2+}$ and H_2O , followed by O–O bond formation (and O_2 release) with a small kinetic barrier. The TS for intramolecular oxo-coupling within $[\text{H}_4\text{Fe}_2\text{O}_7]^{2+}$ is characterized by $\Delta G_{\text{calc}}^\ddagger \cong 4 \text{ kcal mol}^{-1}$. Oxo-coupling within $[\text{H}_3\text{Fe}_2\text{O}_7]^+$ and $\text{H}_2\text{Fe}_2\text{O}_7$ is also predicted to be facile with $\Delta G_{\text{calc}}^\ddagger \cong 6\text{--}7 \text{ kcal mol}^{-1}$. These reactions might be expected if the $\text{p}K_{\text{a}}$ of $[\text{H}_4\text{Fe}_2\text{O}_7]^{2+}$ were very low (i.e., $\ll 1$). Because mono and dianionic forms of diferrate are not expected to exist at low pH, these species were not considered further.

Calculations performed on alternative mechanisms reveal substantially higher $\Delta G_{\text{calc}}^\ddagger$. Barriers vary from 12 to 27 kcal mol^{-1} for water attack involving various diferrate species, indicating that these mechanisms can be excluded from consideration. Water oxidation by monomeric ferrate is also disfavored with $\Delta G_{\text{calc}}^\ddagger$ varying from 21 to 40 kcal mol^{-1} for the relevant protonation states. The observed $\text{D}_2\text{O KIE} \cong 1.0$ is also difficult to reconcile with a water attack mechanism, which should involve significant O–H bond making/breaking. Similarly, the absence of a normal $\text{D}_2\text{O KIE}$ argues against the formation of unbound intermediates such as $^*\text{OH}$ or H_2O_2 .

The comparison of experimental isotope effects to the $^{18}\text{O KIE}_{\text{calc}}$ also favors the oxo-coupling mechanism of diferrate. Although it is not known whether condensation and dimerization of 2 equiv of $[\text{H}_3\text{FeO}_4]^+$ to form $[\text{H}_4\text{Fe}_2\text{O}_7]^{2+}$ and H_2O occurs reversibly, in the kinetic experiments, this reaction is predicted to have a very small $^{18}\text{O EIE}_{\text{calc}} \approx 1.0023$, which falls within the experimental error. Thus, the large normal isotope effect predicted for oxo-coupling within diferrate (~ 1.031) is in agreement with the observed $^{18}\text{O KIE} = 1.027 \pm 0.006$. The higher energy water attack mechanism of $[\text{H}_4\text{Fe}_2\text{O}_7]^{2+}$ is characterized by a much smaller $^{18}\text{O KIE}_{\text{calc}} = 1.0147$. In addition, prohibitively high-energy reaction channels are calculated for $[\text{H}_3\text{FeO}_4]^+$ and H_2FeO_4 , which are associated with $^{18}\text{O KIE}_{\text{calc}}$ for oxo-coupling that are too large and $^{18}\text{O KIE}_{\text{calc}}$ for water attack that are too small to be reconciled with the experimental results.

In our experience, DFT calculations afford more precise isotope effects than free energy barriers. The reason for the discrepancy in $\Delta G_{\text{calc}}^\ddagger$ is likely the approximations made in treating solvation, whereas the error in the $^{18}\text{O KIE}_{\text{calc}}$ is expected to be small given that the calculated structures for reactant and TS, together with the changes in bond force constants, are relatively accurate. A computational error of ± 0.005 , possibly reflective of anharmonicity, has been estimated from temperature-dependent $^{18}\text{O EIEs}$ upon the formation of transition metal superoxide and peroxide complexes from O_2 .^{13,44c,64}

4. Physical Origins of Oxygen-18 Kinetic Isotope Effects. The DFT analysis provides insight concerning the physical origins of isotope effects on O–O bond forming reactions, fundamentally important in natural and artificial water oxidation catalysis. Within the context of eq 7, $^{18}\nu_{\text{RC}}$ and $^{18}K_{\text{TS}}$ contribute to the $^{18}\text{O KIE}_{\text{calc}}$. The DFT calculations in

this study indicate that $^{18}\nu_{\text{RC}}$ is the primary determinant of the large normal competitive $^{18}\text{O KIEs}$ observed. This term is greater than unity because it is defined by the ratio of light to heavy imaginary frequencies. The $^{18}K_{\text{TS}}$ can be inverse or normal. Yet, in most cases analyzed, it is near unity and close to the $^{18}\text{O EIE}$. This observation suggests that the TS and product have similarly mass-dependent vibrational modes.

In the present study, the mass-dependence of the imaginary mode appears to differentiate the TSs for two types of O–O bond-forming reactions. The ability to calculate accurate frequencies and, more importantly, isotopic frequency shifts underscores the importance of using calibrated DFT methods to interpret heavy atom isotope effects. The approach, which involves analyzing all vibrational frequency changes, reproduces $^{18}\text{O EIEs}$ on coordination of O_2 to transition metal centers at varying temperatures¹³ as well as $^{18}\text{O KIEs}$ on H_2O_2 heterolysis and O_2 reductions.⁶⁴ Based on the results reported here, the DFT protocol should be useful for evaluating heavy atom KIEs on a variety of metal-mediated small molecule activation reactions.^{11,13,71–73}

Experimental and computational studies of $^{18}\text{O KIEs}$ on water oxidations by structurally defined inorganic catalysts are now in progress.^{12,13c,74} Findings, thus far, corroborate the results reported here for the model reaction of ferrate, where oxo-coupling via a diferrate intermediate provides a lower energy mechanistic alternative to water attack. The size of the $^{18}\text{O KIE}$ characterizes the TS and serves as a check on the internal consistency of DFT calculations. We note, however, that a more rigorous check on the theory would include analyses of TSs for steps downstream of O–O bond formation. The release of O_2 from an end-on or side-on bound intermediate is one possibility that has been difficult to analyze, as discussed previously,^{13a} apparently requiring the presence of a hydrogen-bond network to activate H_2O for displacement of O_2^{10c} by a concerted or sequential mechanism.^{71c}

In the future, it may be possible to determine $^{18}\text{O KIEs}$ on water oxidation by recombinant PSII from cyano bacteria. Such measurements could illuminate the O–O bond formation mechanism at a new level of detail for comparison to theoretical and spectroscopic models. Though competitive oxygen isotope fractionation has been reported for photosynthetic reactions *in vivo*, interpretations of $^{18}\text{O KIEs}$ are complicated by the very small fractionation factors,^{11,75} which may reflect artifacts caused by unchecked reduction of the O_2 .^{12,76,77}

CONCLUSIONS

This study has delved into the underlying mechanism by which water is oxidized by ferrate. The analysis of the stoichiometric reaction is simpler than catalytic water oxidations, where up to four redox steps can precede and obscure the O–O bond formation step.^{7–9,12,15}

While ^{18}O -labeling experiments require that reactions be investigated under conditions where solvent exchange is slow,¹⁰ this is not true in the case of ferrate.^{10a} Thus, isotope fractionation is applied here to determine competitive $^{18}\text{O KIEs}$ at natural abundance levels and provide mechanistic insight. The results of several independent measurements with multiple preparations of K_2FeO_4 indicate an $^{18}\text{O KIE} = 1.027 \pm 0.006$ at pH 1.0, where kinetic experiments expose a rate constant of $\sim 185 \text{ s}^{-1}$ for oxo-coupling within a preformed di-iron(VI) intermediate. A negligible solvent kinetic isotope effect is observed, consistent with the proposal above and inconsistent

with alternative mechanisms involving rate-limiting proton/hydrogen transfer. Thus, water attack reactions, described here for ferrate and diferrate, as well as the production of $\cdot\text{OH}$ or H_2O_2 in the rate-limiting step can be excluded.

As the solution acidity is decreased, the kinetics of ferrate-mediated water oxidation becomes increasingly complex. A second-order decay process can be resolved with an estimated maximum rate constant of $2.5 \times 10^5 \text{ M}^{-1} \text{ s}^{-1}$ assigned to condensation and dimerization of monomeric ferrate in the rate-limiting step. The putative di-iron(VI) intermediate subsequently undergoes O–O bond formation, accounting for the ^{18}O KIE = 1.022 ± 0.004 . The proposed pathway is consistent with the appearance of inverse solvent isotope effects arising from the $\text{p}K_a$ shift of triprotonated ferrate in D_2O .

All observations are explained using density functional theory, assuming the reaction of the iron(VI) starting material in a triplet state forms an antiferromagnetically coupled μ -1,2-oxo-bridged di-iron(VI) intermediate. Comparisons of experimental and calculated free energy barriers as well as ^{18}O KIEs indicate that intramolecular oxo-coupling within diferrate occurs in preference to intermolecular water attack. Mechanisms involving monomeric ferrate are excludable on the same grounds.

Experimental and computational benchmarks have, thus, been determined for O–O bond formation within a model system containing a reactive ferryl ($\text{Fe}^{\text{VI}}=\text{O}$ or $\text{Fe}^{\text{V}}-\text{O}^*$) that resembles the “dangling” manganyl ($\text{Mn}^{\text{V}}=\text{O}$ or $\text{Mn}^{\text{IV}}-\text{O}^*$) proposed in the oxygen-evolving complex of photosynthetic reaction centers.^{15,18c} The ferrate reaction exhibits a free energy barrier comparable to the enzymatic reaction. Large kinetic barriers to O–O bond formation have been observed for most synthetic water oxidation catalysts that react via six-coordinate geometries.^{7–9,78} The relatively low activation barrier calculated for the di-iron(VI) intermediate, derived from the ferrate, may reflect an intrinsically small inner-sphere reorganization energy associated with coupling terminal oxo ligands in a bridged tetrahedral complex.⁶⁹

■ ASSOCIATED CONTENT

● Supporting Information

Complete ref 38 and further details of the kinetics and DFT calculations. This material is available free of charge via the Internet at <http://pubs.acs.org>.

■ AUTHOR INFORMATION

Corresponding Author

jproth@jhu.edu

Notes

The authors declare no competing financial interest.

■ ACKNOWLEDGMENTS

This work was supported by Grants from the Department of Energy (No. DE-FG02-09ER16094) and Petroleum Research Fund (No. 50046ND3). We are very grateful for assistance provided by Daniel Ashley, Chris Cramer, Mehmed Zahid Ertem, Ben Passey, and Rajeev Prabhakar.

■ REFERENCES

- (1) (a) Woodrow, I. R.; Berry, J. A. *Annu. Rev. Plant Physiol. Plant Mol. Biol.* **1988**, *39*, 533. (b) Brugnoli, E.; Farquhar, G. D. *Adv. Photosynth.* **2000**, *9*, 399.
- (2) (a) Fujishima, A.; Honda, K. *Nature* **1972**, *238*, 37. (b) Calvin, M. *Acc. Chem. Res.* **1978**, *11*, 369. (c) Walter, M. G.; Warren, E. L.;

McKone, J. R.; Boettcher, S. W.; Mi, Q.; Santori, E. A.; Lewis, N. S. *Chem. Rev.* **2010**, *110*, 6446. (d) Gust, D.; Moore, T. A.; Moore, A. L. *Faraday Discuss.* **2012**, *155*, 9. (e) Nocera, D. G. *Acc. Chem. Res.* **2012**, *45*, 767.

(3) Lewis, N. S.; Nocera, D. G. *Proc. Natl. Acad. Sci. U.S.A.* **2006**, *103*, 15729.

(4) (a) Cox, P. M.; Betts, R. A.; Jones, C. D.; Spall, S. A.; Totterdell, L. J. *Nature* **2000**, *408*, 184. (b) Weaver, A. J.; Hillaire-Marcel, C. *Science* **2004**, *304*, 400. (c) Hansen, J.; Sato, M.; Ruedy, R.; Lo, K.; Lea, D. W.; Medina-Elizade, M. *Proc. Natl. Acad. Sci. U.S.A.* **2006**, *103*, 14288.

(5) (a) Berner, R. A. *Nature* **2003**, *426*, 323. (b) Hill, J.; Nelson, E.; Tilman, D.; Polasky, S.; Tiffany, D. *Proc. Natl. Acad. Sci. U.S.A.* **2006**, *103*, 11206. (c) Navarro, R. M.; Pena, M. A.; Fierro, J. L. G. *Chem. Rev.* **2007**, *107*, 3952.

(6) (a) Grätzel, M. *Nature* **2001**, *414*, 338. (b) Balzani, V.; Credi, A.; Venturi, M. *Chem. Sus. Chem.* **2008**, *1*, 26. (c) Tran, P. D.; Artero, V.; Fontecave, M. *Energy Environ. Sci.* **2010**, *3*, 727.

(7) (a) Liu, X.; Wang, F. *Coord. Chem. Rev.* **2012**, *256*, 1115. (b) Clark, A. E.; Hurst, J. K. *Prog. Inorg. Chem.* **2012**, *57*, 1. (c) Concepcion, J. J.; Jurss, J. W.; Brenneman, M. K.; Hoertz, P. G.; Patrocino, A. O. T.; Murakami, I.; Neyde, Y.; Templeton, J. L.; Meyer, T. J. *Acc. Chem. Res.* **2009**, *42*, 1954. (d) Sala, X.; Romero, I.; Rodriguez, M.; Escriche, L.; Llobet, A. *Angew. Chem., Int. Ed.* **2009**, *48*, 2842. (e) Dismukes, G. C.; Brimblecombe, R.; Felton, G. A. N.; Pryadun, R. S.; Sheats, J. E.; Spiccia, L.; Swiegers, G. F. *Acc. Chem. Res.* **2009**, *42*, 1935.

(8) DFT studies of homogeneous inorganic catalysts: (a) Yang, X.; Baik, M. J. *Am. Chem. Soc.* **2006**, *128*, 7476. (b) Yang, X.; Baik, M.-H. *J. Am. Chem. Soc.* **2008**, *130*, 16231. (c) Sartorel, A.; Miro, P.; Salvadori, E.; Romain, S.; Carraro, M.; Scorrano, G.; Di Valentin, M.; Llobet, A.; Bo, C.; Bonchio, M. *J. Am. Chem. Soc.* **2009**, *131*, 16051. (d) Bozoglian, F.; Romain, S.; Ertem, M. Z.; Todorova, T. K.; Sens, C.; Mola, J.; Rodriguez, M.; Romero, I.; Benet-Buchholz, J.; Fontrodona, X.; Cramer, C. J.; Gagliardi, L.; Llobet, A. *J. Am. Chem. Soc.* **2009**, *131*, 15176. (e) Sala, X.; Ertem, M. Z.; Vigar, L.; Todorova, T. K.; Chen, W.; Rocha, R. C.; Aquilante, F.; Cramer, C. J.; Gagliardi, L.; Llobet, A. *Angew. Chem., Int. Ed.* **2010**, *49*, 7745. (f) Wang, L. P.; Wu, Q.; Van Voorhis, T. *Inorg. Chem.* **2010**, *49*, 4543. (g) Hughes, T. F.; Friesner, R. A. *J. Phys. Chem. B* **2011**, *115*, 9280. (h) Bianco, R.; Hay, P. J.; Hynes, J. T. *J. Phys. Chem. A* **2011**, *115*, 8003. (i) Wang, L.-P.; Van Voorhis, T. *J. Phys. Chem. Lett.* **2011**, *2*, 2200. (j) Vilella, L.; Vidossich, P.; Balcells, D.; Lledos, A. *Dalton Trans.* **2011**, *40*, 11241. (k) Polyansky, D. E.; Muckerman, J. T.; Rochford, J.; Zong, R.; Thummel, R. P.; Fujita, E. *J. Am. Chem. Soc.* **2011**, *133*, 14649. (l) Ertem, M. Z.; Gagliardi, L.; Cramer, C. J. *Chem. Sci.* **2012**, *3*, 1293.

(9) DFT studies of homogeneous manganese catalysts as models from PSII: (a) Sproviero, E. M.; Gascón, J. A.; McEvoy, J. P.; Brudvig, G. W.; Batista, V. S. *Coord. Chem. Rev.* **2008**, *252*, 395. (b) McGrady, J. E.; Stranger, R. *Inorg. Chem.* **1999**, *38*, 550. (c) Kuznetsov, A. E.; Geletii, Y. V.; Hill, C. L.; Musaev, D. G. *J. Phys. Chem. A* **2010**, *114*, 11417. (d) Busch, M.; Ahlberg, E.; Panas, I. *Phys. Chem. Chem. Phys.* **2011**, *13*, 15069. (e) Sameera, W. M. C.; McKenzie, C. J.; McGrady, J. E. *Dalton Trans.* **2011**, *40*, 3859.

(10) (a) Goff, H.; Murmann, K. R. *J. Am. Chem. Soc.* **1971**, *93*, 6058. (b) Cape, J. L.; Siems, W. F.; Hurst, J. K. *Inorg. Chem.* **2009**, *48*, 8729. (c) Romain, S.; Bozoglian, F.; Sala, X.; Llobet, A. *J. Am. Chem. Soc.* **2009**, *131*, 2768.

(11) Guy, R. D.; Fogel, M. L.; Berry, J. A. *Plant Physiol.* **1993**, *101*, 37.

(12) Angeles-Boza, A. M.; Roth, J. P. *Inorg. Chem.* **2012**, *51*, 4722.

(13) (a) Roth, J. P. *Acc. Chem. Res.* **2009**, *42*, 399. (b) Smirnov, V. V.; Lanci, M. P.; Roth, J. P. *J. Phys. Chem. A* **2009**, *113*, 1934. (c) Ashley, D. C.; Brinkley, D. W.; Roth, J. P. *Inorg. Chem.* **2010**, *49*, 3661.

(14) Cramer, C. J.; Truhlar, D. G. *Phys. Chem. Chem. Phys.* **2009**, *11*, 10757.

(15) (a) Siegbahn, P. E. M.; Crabtree, R. H. *J. Am. Chem. Soc.* **1999**, *121*, 117. (b) Aullon, G.; Ruiz, E.; Alvarez, S. *Chem.—Eur. J.* **2002**, *8*, 2508. (c) Siegbahn, P. E. M.; Lundberg, M. *Photochem. Photobiol. Sci.*

- 2005, 1035. (d) Sproviero, E. M.; Gascón, J. A.; McEnvoy, J. P.; Brudvig, G. W.; Batista, V. S. *Philos. Trans. R. Soc., B* **2008**, *1494*, 1149. (e) Blomberg, M. R. A.; Siegbahn, P. E. M. *Biochim. Biophys. Acta, Bioenerg.* **2010**, *1797*, 129. (f) Petrie, S.; Stranger, R.; Pace, R. J. *Chem.—Eur. J.* **2010**, *16*, 14026. (g) Rivalta, I.; Brudvig, G. W.; Batista, V. S. *Curr. Opin. Chem. Biol.* **2012**, *16*, 11.
- (16) McEnvoy, J. P.; Brudvig, G. W. *Chem. Rev.* **2006**, *106*, 4455.
- (17) Umena, Y.; Kawakami, K.; Shen, J.-R.; Kamiya, N. *Nature* **2011**, *473*, 55.
- (18) (a) Weng, T.-C.; Hsieh, W.-Y.; Uffelman, E. S.; Gordon-Wylie, S. W.; Collins, T. J.; Pecoraro, V. L.; Penner-Hahn, J. E. *J. Am. Chem. Soc.* **2004**, *126*, 8070. (b) Yano, J.; Robblee, J.; Pushkar, Y.; Marcus, M. A.; Bendix, J.; Workman, J. M.; Collins, T. J.; Solomon, E. I.; DeBeer, G. S.; Yachandra, V. K. *J. Am. Chem. Soc.* **2007**, *129*, 12989. (c) Yano, J.; Yachandra, V. K. *Inorg. Chem.* **2008**, *47*, 1711. (d) McConnell, I. L. *Photosynth. Res.* **2008**, *98*, 261. (e) Brynda, M.; Britt, R. D. In *Metals in Biology: Applications of High Resolution EPR to Metalloenzymes*; Hanson, G., Berliner, L., Eds.; Springer Science: New York, 2010.
- (19) (a) Faller, P.; Goussias, C.; Rutherford, A. W.; Un, S. *Proc. Natl. Acad. Sci. U.S.A.* **2003**, *100*, 8732. (b) Huynh, M. H. V.; Meyer, T. J. *Chem. Rev.* **2007**, *107*, 5004.
- (20) (a) Singh, S.; Debus, R. J.; Wydrzynski, T.; Hillier, W. *Philos. Trans. R. Soc., B* **2008**, *363*, 1229. (b) Beckmann, K.; Messinger, J.; Badger, M. R.; Wydrzynski, T.; Hillier, W. *Photosynth. Res.* **2009**, *102*, 511–52. (c) Shevela, D.; Beckmann, K.; Clausen, J.; Junge, W.; Messinger, J. *Proc. Natl. Acad. Sci. U.S.A.* **2011**, *108*, 3602.
- (21) Mayer, J. M. *Acc. Chem. Res.* **1998**, *31*, 441.
- (22) (a) Sharma, V. K. *Adv. Environ. Res.* **2002**, *6*, 143–156. (b) Sharma, V. K. *Chemosphere* **2008**, *73*, 1379. (c) Macova, Z.; Bouzek, K.; Hives, J.; Sharma, V. K.; Terry, R. J.; Baum, J. C. *Electrochim. Acta* **2009**, *5410*, 2673.
- (23) (a) Wagner, B.; Reinen, D.; Brunold, T. C.; Güdel, H. U. *Inorg. Chem.* **1995**, *34*, 1934. (b) Tsapin, A.; Goldfeld, M.; Neelson, K. *Icarus* **2000**, *147*, 68.
- (24) (a) Lee, J.; Tryk, D. A.; Fujishima, A.; Park, S.-P. *Chem. Commun.* **2002**, *5*, 486. (b) Villanueva-Rodriguez, M.; Sanchez-Sanchez, C. M.; Montiel, V.; Brillas, E.; Peralta-Hernandez, J. M.; Hernandez-Ramirez, A. *Electrochim. Acta* **2012**, *64*, 196.
- (25) Betley, T. A.; Wu, J.; Van Voorhis, T.; Nocera, D. G. *Inorg. Chem.* **2008**, *47*, 1849.
- (26) (a) Licht, S.; Wang, B.; Ghosh, S. *Science* **1999**, *285*, 1039. (b) Licht, S.; Yu, X. *ACS Symp. Ser.* **2008**, *985*, 197.
- (27) (a) Griffith, W. P. *J. Chem. Soc. A* **1966**, 1467. (b) Audette, R. J.; Quail, J. W. *Inorg. Chem.* **1972**, *11*, 1904. (c) Hoppe, M. L.; Schlemper, E. O.; Murmann, R. K. *Acta Crystallogr.* **1982**, *B38*, 2237. (d) Lia, C.; Lia, X. Z.; Graham, N. *Chemosphere* **2005**, *61*, 537.
- (28) Wood, R. H. *J. Am. Chem. Soc.* **1958**, *80*, 2038.
- (29) (a) Carr, J. D.; Kelter, P. B.; Tabatabai, A.; Spichal, D.; Erickson, J.; Mclaughlin, C. W. In *Water Chlorination: Chemistry, Environmental Impact, and Health Effects*; Jolley, R. L., Bull, R. J., Davis, W. P., Katz, S., Roberts, M. H., Jr., Jacobs, V. A., Eds.; Lewis Publishers Inc.: Chelsea, MI, 1985; Vol. 5. (b) Carr, J. D. In *Ferrates: Synthesis, Properties, and Applications in Water and Wastewater Treatment*; Sharma, V. K., Ed.; ACS Symposium Series 985; American Chemical Society: Washington, DC, 2008; p 189.
- (30) Rush, J. D.; Zhao, Z.; Bielski, B. H. J. *Free Radical Res.* **1996**, *24*, 187.
- (31) (a) Pestovsky, O.; Bakac, A. *Inorg. Chem.* **2006**, *45*, 814. (b) Pestovsky, O.; Stoian, S.; Bominaar, E. L.; Shan, X.; Munck, E.; Que, L., Jr.; Bakac, A. *Angew. Chem., Int. Ed.* **2005**, *44*, 6871. (c) Pestovsky, O.; Bakac, A. *J. Am. Chem. Soc.* **2004**, *126*, 13757.
- (32) A recent description of iron-mediated water oxidation catalysis is presented in Fillol, J. L.; Codola, Z.; Garcia-Bosch, I.; Gomez, L.; Pla, J. J.; Costas, M. *Nat. Chem.* **2011**, *3*, 807.
- (33) (a) Rush, J. D.; Bielski, B. H. J. *Inorg. Chem.* **1994**, *33*, 5499. (b) Sharma, V. K.; Burnett, C. R.; O'Connor, D. B.; Cabelli, D. *Environ. Sci. Technol.* **2002**, *36*, 4182. (c) Sharma, V. K.; Cabelli, D. J. *Phys. Chem. A* **2009**, *113*, 8901–8906. (d) Sharma, V. K. *J. Environ. Manage.* **2011**, *92*, 1051.
- (34) Marcel, M.; Zuberbuehler, A. D. *Anal. Chem.* **1990**, *62*, 2220.
- (35) (a) Manner, V. M.; Markle, T. F.; Freudenthal, J. H.; Roth, J. P.; Mayer, J. M. *Chem. Commun.* **2008**, 256. (b) Yamauchi, J.; Katayama, A.; Tamada, M.; Tanaka, S. *Appl. Magn. Reson.* **2000**, *18*, 249.
- (36) Epstein, S.; Mayeda, T. *Geochim. Cosmochim. Acta* **1953**, *4*, 213.
- (37) Coplen, T. B. *Nature* **1995**, *375*, 285.
- (38) Frisch, M. J.; et al. *Gaussian 09*, Revision A.02; Gaussian, Inc., Wallingford CT, 2009.
- (39) (a) Perdew, J. P.; Wang, Y. *Phys. Rev. B* **1986**, *33*, 8800. (b) Perdew, J. P. In *Electronic Structure of Solids '91*; Ziesche, P., Eschrig, H., Eds.; Akademie Verlag: Berlin, Germany, 1991; p 11. (c) Adamo, C.; Barone, V. *J. Chem. Phys.* **1998**, *108*, 664.
- (40) Hehre, W. J.; Radom, L.; Schleyer, P. v. R.; Pople, J. A. *Ab Initio Molecular Orbital Theory*; Wiley: New York, 1986.
- (41) Stevens, W. J.; Krauss, M.; Basch, H.; Jasien, P. G. *Can. J. Chem.* **1992**, *70*, 612.
- (42) Marenich, A. V.; Cramer, C. J.; Truhlar, D. G. *J. Phys. Chem. B* **2009**, *113*, 6378.
- (43) Cramer, C. J. *Essentials of Computational Chemistry*, 2nd ed. Wiley: West Sussex, U.K., 2004.
- (44) (a) Noodleman, L.; Norman, J. G. *J. Chem. Phys.* **1979**, *70*, 4903–4906. (b) Yamaguchi, K.; Jensen, F.; Dorigo, A.; Houk, K. N. *Chem. Phys. Lett.* **1988**, *149*, 537. (c) Lanci, M. P.; Smirnov, V. V.; Cramer, C. J.; Gauchenova, E. V.; Sundermeyer, J.; Roth, J. P. *J. Am. Chem. Soc.* **2007**, *129*, 14697.
- (45) Al-Abdalla, A.; Seijo, L.; Barandiarán, Z. *J. Chem. Phys.* **1998**, *109*, 6396.
- (46) Bigeleisen, J.; Goepfert-Mayer, M. *J. Chem. Phys.* **1947**, *15*, 261.
- (47) Wolfsberg, M.; Van Hook, W. A.; Paneth, P.; Rebelo, L. P. N. *Isotope Effects in the Chemical, Geochemical and BioSciences*; Springer: New York, 2010.
- (48) See the Supporting Information for details.
- (49) Several studies have assessed the apparent molar extinction coefficients at variable pH. See refs 29, 30, and 33d.
- (50) Junk, P. C.; McCool, B. J.; Moubaraki, B.; Murray, K. S.; Spiccia, L.; Cahion, J. D.; Steed, J. W. *J. Chem. Soc., Dalton Trans.* **2002**, 1024.
- (51) Mulay, L. N.; Selwood, P. W. *J. Am. Chem. Soc.* **1955**, *77*, 2693.
- (52) Lente, G.; Fábán, I. *Inorg. Chem.* **1999**, *38*, 603.
- (53) (a) Drago, R. S. *Physical Methods for Chemists*, 2nd ed.; Surfside Publishers: Gainesville, FL, 1992; p 583. (b) Symons, M. C. R.; Gutteridge, J. M. C. *Free Radicals and Iron: Chemistry Biology and Medicine*; Oxford University Press: Oxford, 1998. (c) Levanon, H.; Stein, G.; Luz, Z. *J. Chem. Phys.* **1970**, *53*, 876.
- (54) Conocchioli, T. J.; Hamilton, E. J.; Sutin, N. *J. Am. Chem. Soc.* **1965**, *87*, 926.
- (55) Evidence was obtained for iron(II) by adding chelating agents that form a known chromophore to ferrate solutions under acidic conditions, as described in ref 29.
- (56) Jeannot, C.; Malaman, B.; Gérardin, R.; Oulladiaf, B. *J. Solid State Chem.* **2002**, *165*, 266.
- (57) Solvent KIEs have been observed for O–O bond formation (concomitant with H transfer) in a single-site ruthenium catalyst: Chen, Z.; Concepcion, J. J.; Hu, X.; Yang, W.; Hoertz, P. G.; Meyer, T. *J. Proc. Natl. Acad. Sci. U.S.A.* **2010**, *107*, 7225.
- (58) O'Leary, M. H. *Phytochemistry* **1981**, *20*, 553. A derivation of the ^{18}O KIE @ $R_{\text{H}_2\text{O}}/R_{\text{O}_2}$ is provided in the Supporting Information of ref 12.
- (59) (a) Goldberg, N. R.; Tewari, Y. B. *J. Chem. Thermodyn.* **2002**, *34*, 821. (b) Nakazato, T.; Yoza, N.; Ishiguro, S.-I. *J. Chem. Soc., Faraday. Trans.* **1997**, *93*, 4295.
- (60) (a) Chang, S. G.; Littlejohn, D.; Hu, K. Y. *Science* **1987**, *237*, 756. (b) Dyekjir, J. D.; Berg, R. W.; Johansen, H. *J. Phys. Chem. A* **2003**, *107*, 5826.
- (61) Hoffmann, M. M.; Darab, J. G.; Fulton, J. L. *J. Phys. Chem. A* **2001**, *105*, 1772. (b) Swinehart, J. H.; Castellan, G. W. *Inorg. Chem.* **1964**, *3*, 278.
- (62) (a) Holyer, R. H.; Baldwin, H. W. *Can. J. Chem.* **1967**, *45*, 413. (b) Pladzewicz, J. R.; Espenson, J. H. *Inorg. Chem.* **1971**, *10*, 634.

(63) Brito, F.; Ascanio, J.; Mateoa, S.; Hernández, C.; Araujo, L.; Gili, P.; Martín-Zarzab, P.; Domínguez, S.; Mederos, A. *Polyhedron* **1997**, *16*, 3835.

(64) Similar approaches were utilized in (a) Roth, J. P.; Cramer, C. J. *J. Am. Chem. Soc.* **2008**, *130*, 7802. (b) Huff, G. S.; Doncheva, I. S.; Brinkley, D. W.; Angeles-Boza, A. M.; Mukherjee, A.; Cramer, C. J.; Roth, J. P. *Biochemistry* **2011**, *50*, 7375.

(65) A similar transition state has been proposed for the photochemical reaction of $[\text{Mn}^{\text{VI}}\text{O}_4]^-$ that produces O_2 , possibly via an η^2 -peroxo intermediate. Lee, D. G.; Moylan, C. R.; Hayashi, T.; Brauman, J. I. *J. Am. Chem. Soc.* **1987**, *109*, 3003.

(66) Barriers ca. 10 kcal mol⁻¹ lower have been predicted for inner-sphere reactions of alcohols and cyanide (a) Ohta, T.; Kamachi, T.; Shiota, Y.; Yoshizawa, K. *J. Org. Chem.* **2001**, *66*, 4122. (b) Kamachi, T.; Kouno, T.; Yoshizawa, K. *J. Org. Chem.* **2005**, *70*, 4380. (c) Kamachi, T.; Nakayama, T.; Yoshizawa, K. *Bull. Chem. Soc. Jpn.* **2008**, *81*, 1212.

(67) Related approaches have been applied in isotopic studies of enzyme and small molecule reactions: (a) Cleland, W. W. *Methods Enzymol.* **1995**, *249*, 341. (b) Berti, P. J. *Methods Enzymol.* **1999**, *308*, 355. (c) Schramm, V. L. *Acc. Chem. Res.* **2003**, *36*, 588. (d) Schramm, V. L. *Curr. Opin. Chem. Biol.* **2007**, *11*, 529. (e) Ralph, E. C.; Hirschi, J. S.; Anderson, M. A.; Cleland, W. W.; Singleton, D. A.; Fitzpatrick, P. F. *Biochemistry* **2007**, *46*, 7655. (f) Delmonte, A. J.; Haller, J.; Houk, K. N.; Sharpless, K. B.; Singleton, D. A.; Strassner, T.; Thomas, A. A. *J. Am. Chem. Soc.* **1997**, *119*, 9907. (g) Singleton, D. A.; Hang, C.; Szymanski, M. J.; Meyer, M. P.; Leach, A. G.; Kuwata, K. T.; Chen, J. S.; Greer, A.; Foote, C. S.; Houk, K. N. *J. Am. Chem. Soc.* **2003**, *125*, 1319. (h) Slaughter, L. M.; Wolczanski, P. T.; Klinckman, T. R.; Cundari, T. R. *J. Am. Chem. Soc.* **2000**, *122*, 7953. (i) Parkin, G. *Acc. Chem. Res.* **2009**, *42*, 315. (j) Gonzalez-James, O. M.; Zhang, X.; Datta, A.; Hrovat, D. A.; Borden, W. T.; Singleton, D. A. *J. Am. Chem. Soc.* **2010**, *132*, 12548.

(68) Water attack upon $\text{H}_2\text{Fe}_2\text{O}_7$ is predicted to have an unattainable barrier, ca. 20 kcal mol⁻¹ higher than that predicted for $[\text{H}_4\text{Fe}_2\text{O}_7]^{2+}$, but an ¹⁸O KIE = 1.0352, just outside the experimental error.

(69) Marcus, R. A.; Sutin, N. *Biochim. Biophys. Acta* **1985**, *811*, 265.

(70) The adiabatic approximation gives the upper bounds to ΔG^\ddagger based upon the expression: $k_{\text{uni}} = \kappa k_{\text{B}}T/h \exp(-\Delta G^\ddagger/(RT))$; where k_{B} and h are Boltzmann's and Planck's constants, T is temperature, and κ , the transmission coefficient, is assumed to be unity causing the pre-exponential term to approach the frequency of a bond vibration ($\sim 10^{13} \text{ s}^{-1}$).

(71) (a) Lanci, M. P.; Brinkley, D. W.; Stone, K. L.; Smirnov, V. V.; Roth, J. P. *Angew. Chem., Int. Ed.* **2005**, *44*, 7273. (b) Lanci, M. P.; Roth, J. P. *J. Am. Chem. Soc.* **2006**, *128*, 16006. (c) Popp, B. V.; Wendlandt, J. E.; Landis, C. R.; Stahl, S. S. *Angew. Chem., Int. Ed.* **2007**, *46*, 601.

(72) Roth, J. P.; Klinman, J. P. In *Isotope Effects in Chemistry and Biology*; Kohen, A.; Limbach, H.-H., Eds.; CRC Press: Boca Raton, FL, 2006.

(73) (a) Sra, A. K.; Hu, Y.; Martin, G. E.; Snow, D. D.; Ribbe, M. W.; Kohen, A. *J. Am. Chem. Soc.* **2004**, *126*, 12768. (b) Laplaza, C. E.; Johnson, M. J. A.; Peters, J.; Odom, A. L.; Kim, E.; Cummins, C. C.; George, G. N.; Pickering, I. J. *J. Am. Chem. Soc.* **1996**, *118*, 8623.

(74) Roeske, C. A.; O'Leary, M. H. *Biochemistry* **1984**, *23*, 6275. (b) Tcherkez, G.; Farquhar, G. D. *Funct. Plant Biol.* **2005**, *32*, 277.

(75) Roth, J. P.; Angeles-Boza, A. M.; Ertem, M. Z.; Sarma, R.; Maji, S.; Llobet, A.; Cramer, C. J. manuscript in preparation.

(76) (a) Burda, K.; Bader, K. P.; Schmid, G. H. *Biochim. Biophys. Acta* **2003**, *1557*, 77. (b) Metzner, H.; Fischer, K.; Bazlen, O. *Biochim. Biophys. Acta Bioenerg.* **1979**, *548*, 287.

(77) Eisenstadt, D.; Barkan, E.; Luz, B.; Kaplan, A. *Photosynth. Res.* **2010**, *103*, 97.

(78) A homogenous ruthenium catalyst with activity that rivals natural photosystem II has been reported: Duan, L.; Bozoglian, F.; Mandal, S.; Stewart, B.; Privalov, T.; Llobet, A.; Sun, L. *Nat. Chem.* **2012**, *4*, 418.